

DRAFT VERSION NOVEMBER 25, 2021

Typeset using L^AT_EX **preprint** style in AASTeX61

THE DISTANCE AND THE NEAR-IR EXTINCTION OF THE MONOCEROS SUPERNOVA REMNANT

HE ZHAO,¹ BIWEI JIANG,¹ SHUANG GAO,¹ JUN LI,¹ AND MINGXU SUN¹

¹*Beijing Normal University*

(Accepted by ApJ February 1, 2018)

ABSTRACT

Supernova remnants (SNRs) embody the information of the influence on dust properties by the supernova explosion. Based on the color indexes from the 2MASS photometric survey and the stellar parameters from the SDSS–DR12/APOGEE and LAMOST–DR2/LEGUE spectroscopic surveys, the near-infrared extinction law and the distance of the Monoceros SNR are derived together with its nearby two nebulae – the Rosette Nebula and NGC 2264. The distance is found at the position of the sharp increase of interstellar extinction with distance and the nebular extinction is calculated by subtracting the foreground interstellar extinction. The distance of the Monoceros SNR is determined to be 1.98 kpc, larger than previous values. Meanwhile, the distance of the Rosette Nebula is 1.55 kpc, generally consistent with previous work. The distance between these two nebulae suggests no interaction between them. The distance of NGC 2264, 1.20 kpc, exceeds previous values. The color excess ratio, $E_{\text{JH}}/E_{\text{JKs}}$, is 0.657 for the Monoceros SNR, consistent with the average value 0.652 for the Milky Way (Xue et al. 2016). The consistency is resulted from that the SNR material is dominated by interstellar dust rather than the supernova ejecta. $E_{\text{JH}}/E_{\text{JKs}}$ equals to 0.658 for the Rosette Nebula, further proving the universality of the near-infrared extinction law.

Keywords: ISM: supernova remnants - dust, extinction - infrared: ISM - stars: distances

Corresponding author: Biwei Jiang

bjiang@bnu.edu.cn

hezhaoh@mail.bnu.edu.cn

sgao@bnu.edu.cn

lijun@mail.bnu.edu.cn

mxsun@mail.bnu.edu.cn

1. INTRODUCTION

A leading school of the origin of interstellar dust (ISD) is the envelopes of low mass stars during their asymptotic giant branch (AGB) stage. But with the discovery of large amount of dust in the galaxies at high red shifts (Maiolino et al. 2004; Watson et al. 2015) and in the Galactic (Gomez et al. 2012; Owen & Barlow 2015; Biscaro & Cherchneff 2016; De Looze et al. 2017) and extra-galactic supernova remnants (SNRs) such as SN1987A (Matsuura et al. 2011; Indebetouw et al. 2014; Wesson et al. 2015; Bevan & Barlow 2016) and others (Temim et al. 2017; Bocchio et al. 2016; Bevan et al. 2017), supernovae (SNe) are thought to be more important than before in alleviating the dust budgetary problem (e.g., Matsuura et al. 2009; Dunne et al. 2011). Dust formed in the explosive ejecta of SNe disperses into the interstellar medium (ISM) in the phase of SNR. Theoretical computation demonstrates that small grains may be completely destroyed by reverse shock, but very large grains can be survival and dispersed into ISM without significantly decreasing their sizes (Nozawa et al. 2007). The amount of dust formed by SNe is largely a topic of much debate. Considering all estimations in the literatures, the dust mass of Cassiopeia A (Cas A) SNR has an uncertainty of two orders of magnitude, from $\sim 10^{-3} M_{\odot}$ (Hines et al. 2004) to $\sim 0.5 M_{\odot}$ (De Looze et al. 2017). For recent works, Barlow et al. (2010) derived a cool (~ 35 K) dust component with a mass of $0.0075 M_{\odot}$. Arendt et al. (2014) found $\lesssim 0.1 M_{\odot}$ cold dust in the unshocked ejecta. De Looze et al. (2017) also identified a concentration of cold dust in the unshocked region and derived a mass of $0.3 - 0.5 M_{\odot}$ of silicate grains, with a lower limit of $\geq 0.1 M_{\odot}$. Although these values are in better agreement because of more sophisticated techniques and better data, the estimation of dust mass is still a difficult job. Because the majority of dust in SNRs is cold and thus radiating weakly in the far infrared (FIR), its radiation can hardly be detected. It is therefore hard to estimate the mass of dust produced by SNe when one is only detecting warm dust that makes up just a small fraction of the total dust (usually two orders lower than the cold component, Gomez et al. 2012; De Looze et al. 2017). Bevan & Barlow (2016) present an alternative method. They study the late-time optical and near-infrared (NIR) line profiles of SNRs, which will exhibit a red-blue asymmetry as a result of greater extinction produced by the internal dust. Bevan et al. (2017) applied this approach to estimate dust mass for three SNRs, and gave an estimate of $\sim 1.1 M_{\odot}$ for Cas A. The technique we adopt in this paper also exploits the extinction effects of dust rather than its infrared emission in order to trace all of the dust (both warm and cold components). Our approach is based on the fundamental principle that absolute extinction is proportional to dust mass.

The Monoceros Nebula (G205.5 +0.5) is an old (1.5×10^5 yr; Graham et al. 1982) nebulous object that is firstly verified to be a SNR by the fine filamentary structure observed in the Palomar Sky Atlas red plates and the non-thermal radio emission at 237 MHz and 1415 MHz (Davies 1963). It lies between the Rosette Nebula (southeast) and NGC 2264 (north). It has the largest angular diameter, $220'$, among the Galactic SNRs (Green 2014). Table 1 presents its position, lying almost in the midplane of the Milky Way, together with that of the Rosette Nebula and NGC 2264 that are slightly above the Galactic plane.

The Monoceros SNR has been observed in almost complete wavebands, from gamma-ray to radio. With the observation of FERMI/LAT, Katagiri et al. (2016) suggest that the gamma-ray emission from the Monoceros SNR is dominated by the decay of π^0 produced by the interaction of shock-accelerated protons with the ambient matter. Leahy et al. (1986) finds that the X-ray bright regions correlate well with the bright optical filaments, but none of his six point sources seems to be a

neutron star. In optics, it appears that there are two distinct parts: one is diffuse in the center and the other is a filamentary structure along the edge of the remnant (Davies et al. 1978). Based on the observations at $60\ \mu\text{m}$, 6 cm, 11 cm, and 21 cm, a new southern shell branch and a western strong regular magnetic field are found in the region of Monoceros (Xiao & Zhu 2012).

Near the Monoceros SNR, the Rosette Nebula is a large H II region located near a giant molecular cloud, associated with the open cluster NGC 2244. It appears that the Rosette Nebula is overlapped with the filamentary structure of Monoceros in the southeast (Davies 1963). North of the Monoceros SNR, NGC 2264 contains two astronomical objects: the Cone Nebula, an H II region located in the southern part, and the northern part named Christmas Tree Cluster. The Cone's shape comes from a dark absorption nebula consisting of cold molecular hydrogen and dust. The region of Cone Nebula and the cluster is very small (about $20'$ in diameter), but there seems to be a much larger dust cloud surrounding them. The rim of the cloud extends southward to the edge of Monoceros. This is supported by Davies et al. (1978) and the observation of IRAS (Infrared Astronomical Satellite; Neugebauer et al. 1984; Wheelock et al. 1994) at $60\ \mu\text{m}$ (Figure 1).

The distances of the three nebulas are not certainly determined. By making use of the empirical surface brightness - diameter relation (the $\Sigma - D$ relation) (Mills 1974), Davies et al. (1978) estimates a distance of Monoceros as $1.6 \pm 0.3\text{ kpc}$. Other studies result in 1.5 kpc (Leahy et al. 1986) and 1.6 kpc (Graham et al. 1982) (with the same $\Sigma - D$ relation, but different values of parameters). For the two neighbouring nebulas, the distance of NGC 2264 is around 0.8 kpc , as determined to be 0.715 kpc (Becker & Fenkart 1963), 0.8 kpc (Walker 1956), and 0.95 kpc (Morgan et al. 1965). For Rosette Nebula, the results are highly dispersive, 1.66 kpc (Johnson 1962), 1.7 kpc (Morgan et al. 1965), and 2.2 kpc (Becker & Fenkart 1963). From the measurement of $\text{H}\alpha$, Davies et al. (1978) presents a systematic change of heliocentric radial velocities (V_{HEL}) from north to south, which gives some clues concerning their relative distances, and suggests that there may be interaction between Monoceros and Rosette, while NGC 2264 is in front of them. Xiao & Zhu (2012) also suggests that Monoceros has probably triggered part of the star formation in the Rosette Nebula.

In this work, we try to determine both the extinction and the distance simultaneously of the Monoceros SNR by measuring the corresponding parameters of a number of stars in its sightline. In the same time, the extinction and distances are determined for the two neighbouring nebulas, Rosette Nebula and NGC 2264. Stellar extinction will increase sharply when meeting with nebula due to the higher dust density than the diffuse medium, therefore, the distance to the nebula can then be found from the position where the extinction increases sharply. The main steps are shown as following:

1. We determine the relation between intrinsic color index in the NIR and stellar effective temperature, and use it to calculate the NIR extinction and color excess for each star.
2. Absolute magnitudes and distances of individual stars are calculated based on stellar parameters and photometry by using the PARSEC model.
3. The distances to the Monoceros SNR, as well as Rosette Nebula and NGC 2264, are derived according to position of the sharply increased extinction along the line of sights.
4. The extinction produced by the SNR and the other two nebulas is derived by subtracting the foreground extinction. The color excess ratio, $E_{\text{JH}}/E_{\text{JKs}}$ is used to describe the NIR extinction law.

Table 1. The geometrical information of the three targets

Object	RA	DEC	GLON	GLAT	Angular diameter
	(h:m)	(d:m)	(deg)	(deg)	(arcmin)
Monoceros	6 39	6 30	205.73	0.21	220
Rosette	6 34	5 00	206.47	-1.65	78
NGC 2264	6 41	9 53	202.95	2.20	20

5. A rough estimation of the dust mass in the SNR is derived from its extinction.

In Section 2, the data sets and quality controls are described. We determine the extinction and distance of individual star in Section 3. We use these results to estimate the distances of the three nebulae in Section 4. The near-infrared extinction law is derived in Section 5. We estimate the dust mass in the region of Monoceros SNR according to its extinction in Section 6. Finally, we summarize the results and implications of this study in Section 7.

2. DATA AND QUALITY CONTROL

In order to complete the task, the near-infrared photometric data is taken from 2MASS, and the stellar parameters are taken from the spectroscopic surveys – SDSS–DR12/APOGEE and LAMOST–DR2/LEGUE.

2.1. Data

2.1.1. 2MASS

The *Two Micron All Sky Survey* (2MASS) is an all-sky photometric survey in the near-infrared bands JHK_S (Cohen et al. 2003). There are over 470 million stars in the 2MASS All-Sky Point Source Catalog (Cutri et al. 2003).

2.1.2. APOGEE

As one of the four experiments in the Sloan Digital Sky Survey III (SDSS–III), *Apache Point Observatory Galactic Evolution Experiment* (APOGEE) is a high-resolution ($R \approx 22,500$), near-infrared (H –band, $1.51\,\mu\text{m} - 1.70\,\mu\text{m}$) spectroscopic survey with high signal-to-noise ratio (about 85% stars with $S/N > 100$) of more than 100,000 Galactic red giant stars. APOGEE measures stellar parameters, including effective temperature T_{eff} , surface gravity $\log g$, and metallicity $[M/H]$. The most recently released APOGEE catalog we use contains 163,278 stars (Eisenstein et al. 2011; Alam et al. 2015).

2.1.3. LEGUE

The Large Sky Area Multi-Object fiber Spectroscopic Telescope (LAMOST) is a Chinese national scientific research facility operated by National Astronomical Observatories, Chinese Academy of Science (NAOC). LAMOST is a reflecting Schmidt telescope with a $5.72\,\text{m} \times 4.40\,\text{m}$ Schmidt mirror (MA) and a $6.67\,\text{m} \times 6.05\,\text{m}$ primary mirror (MB). Both MA and MB are segmented. The unique design of LAMOST enables it to obtain 4,000 spectra in a single exposure to a limiting magnitude as faint as $r = 19$ at the resolution $R = 1800$ with the wavelength coverage of

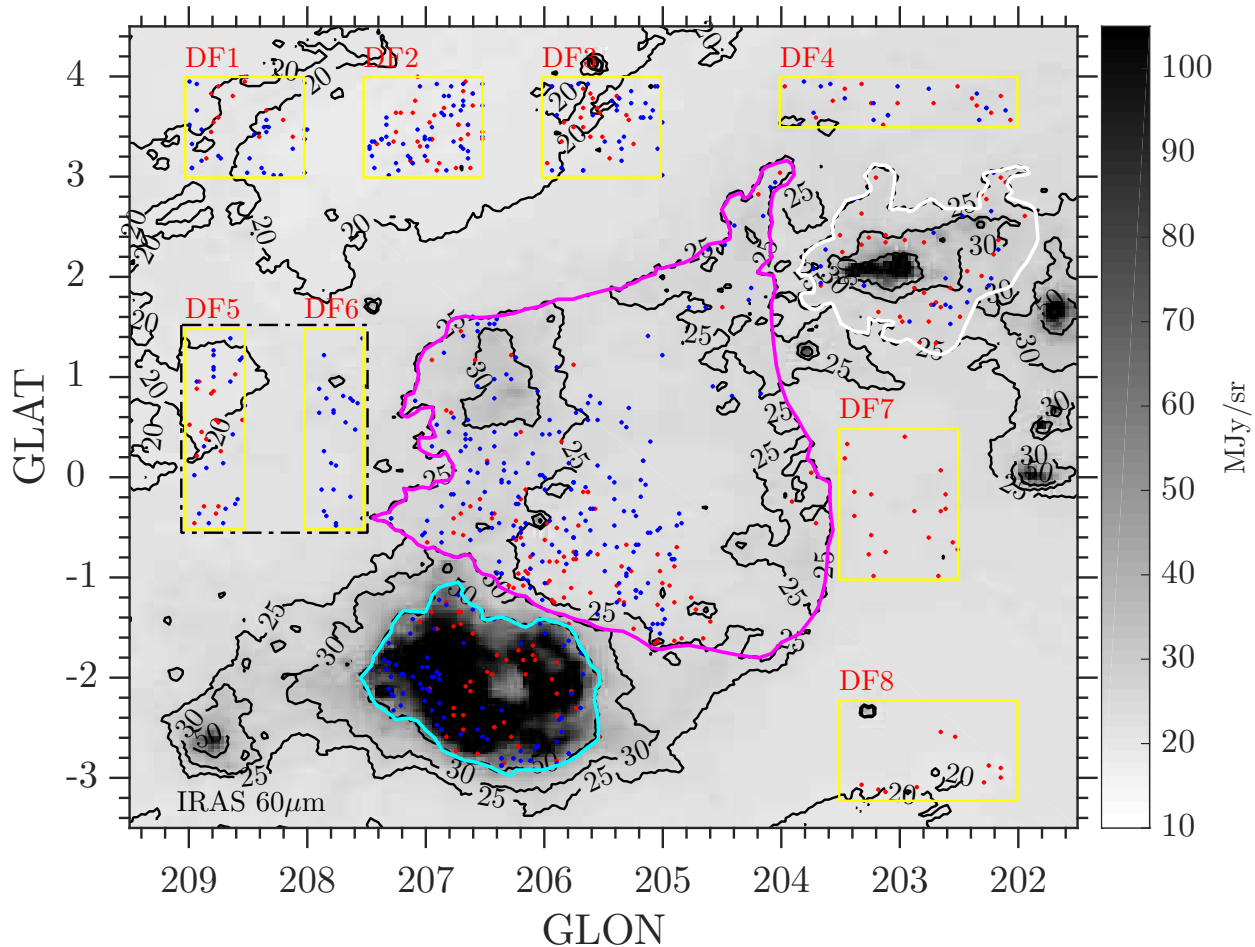


Figure 1. The contours of the IRAS $60\,\mu\text{m}$ image of the target region centered on (Gal: $205^{\circ}5, +0^{\circ}5$). The ISM background emission in the Galactic plane is about $20 - 25\,\text{MJy/sr}$. The emission from dust in Monoceros SNR is $25 - 40\,\text{MJy/sr}$, apparently higher than adjacent ISM. Meanwhile the emission from compact regions of the Rosette Nebula and NGC 2264 are both over $50\,\text{MJy/sr}$, with the maximum reaching about $250\,\text{MJy/sr}$. The blue and red dots are the tracers (see Section 2.3) – dwarfs and giants in the selected regions, respectively. The magenta, cyan and white lines are the borders of Monoceros SNR, Rosette Nebula and NGC 2264, respectively. The yellow lines are the borders of eight diffuse regions. Additionally, the black dot dash lines, surrounding DF5 and DF6, enclose the reference region mentioned in Section 4.1.

$3700 < \lambda < 9100\,\text{\AA}$ (Zhao et al. 2012). The *LAMOST Experiment for Galactic Understanding and Exploration* (LEGUE) survey is one of its two key projects, observing both dwarf and giant stars that are used as extinction tracers in this work. LAMOST–DR2/LEGUE, with stellar parameters, i.e. T_{eff} , $\log g$, $[\text{Fe}/\text{H}]$, was released in 2015 and contained more than two million sources (Deng et al. 2012; Deng 2014), which is the dataset we use.

2.2. Data Quality Control

In order to determine both the extinction and distance of the Monoceros SNR, as well as NGC 2264 and the Rosette Nebula, dwarfs and giants are chosen as extinction tracers and distance indicators mainly because their intrinsic colors are well determined by Jian et al. (2017) and Xue et al. (2016).

The preliminary operation combines near-infrared photometry with stellar parameters. The data is collated by matching the sources from 2MASS point source catalog and LAMOST/DR2 within $1''$. Meanwhile, the APOGEE catalog already includes the 2MASS photometry since the APOGEE survey was based on 2MASS.

The data quality is controlled for a precise result. The stars are picked up only if they have full information of photometry in all the JHK_S bands and of stellar parameters T_{eff} , $\log g$ and $[\text{Fe}/\text{H}]$. Although APOGEE measures $[\text{M}/\text{H}]$ instead of $[\text{Fe}/\text{H}]$, [Mészáros et al. \(2013\)](#) points out that $[\text{M}/\text{H}]$ is generally close to $[\text{Fe}/\text{H}]$. Therefore we assume that $[\text{M}/\text{H}]$ is equivalent to $[\text{Fe}/\text{H}]$. The measurements are required to fulfill the following criteria.

1. The photometric error of the JHK_S bands, $\sigma_{JHK_S} < 0.05$ mag.
2. The errors of stellar parameters from LEGUE, $\sigma_{T_{\text{eff}}} < 300$ K, $\sigma_{\log g} < 0.5$ dex, and $\text{snrg} > 30$ (signal-to-noise ratio in the g -band).
3. The errors of stellar parameters from APOGEE, $\sigma_{T_{\text{eff}}} < 300$ K, $\sigma_{\log g} < 0.2$ dex, and $\text{S/N} > 100$. In addition, the velocity scattering of multi-epoch measurements, $\text{VSCATTER} < 0.3$ km/s to exclude binary stars.

The different criterion in $\log g$ for LEGUE and APOGEE is caused by the much higher accuracy of APOGEE than LEGUE by its much higher spectral resolution.

Furthermore, the dwarf and giant stars are chosen according to the following criteria:

1. $4000 \text{ K} < T_{\text{eff}} < 7000 \text{ K}$ for dwarfs because of relatively uncertain parameters at both lower and higher effective temperatures for the LAMOST/DR2 catalog. $4000 \text{ K} < T_{\text{eff}} < 5200 \text{ K}$ for G- and K-type red giants for which the intrinsic near-infrared colors are well determined by [Xue et al. \(2016\)](#). Although G- and K-type giants have a T_{eff} range extending to 3600 K, but most giants with $3500 \text{ K} < T_{\text{eff}} < 4000 \text{ K}$ have $\log g < 1$, i.e. they are red supergiants.
2. $\log g > 4$ for dwarfs, and $1 < \log g < 3$ for giants. [Worley et al. \(2016\)](#) set a value of $\log g = 3.5$ as the boundary of giant and dwarf. Taking the typical value of $\Delta \log g$ of LEGUE (~ 0.5 dex) into account, [Jian et al. \(2017\)](#) shifted the boundary and stars with $3 < \log g < 4$ are dropped to avoid ambiguity, which has little effect on the result thanks to the numerous stars in the database.
3. $-0.5 < [\text{Fe}/\text{H}] < 0.5$ for both dwarfs and giants. Both metal-poor and metal-rich stars are removed to reduce the influence of metallicity on intrinsic colors in near-infrared bands. Moreover, this range of metallicity is much precisely determined.

Under these criteria, 374,052 dwarfs and 90,741 giants (45,444 from LEGUE and 45,297 from APOGEE) are selected to consist the star sample for our study of the relation between stellar intrinsic colors and effective temperatures.

Based on our criteria, stars fainter than $K_S = 14.4$ mag will be excluded, most of which are far away or highly obscured by dust. But our star sample can still reach as far as 8 kpc, most within 6 kpc, covering the three targets (around 2 kpc). Additionally, it is enough to trace the extinction of the faint SNR. Meanwhile, such depth may be unable to trace the dense regions of the three nebulae.

Table 2. Number of stars in each selected nebular regions and eight diffuse fields (DFs) (cf. Figure 1).

	Monoceros	Rosette	NGC 2264	DF1	DF2	DF3	DF4	DF5	DF6	DF7	DF8
Dwarf	194	97	23	28	53	34	17	23	25	0	0
Giant	85	47	33	13	33	20	15	17	0	19	10
Total	279	144	56	41	86	54	32	40	25	19	10

2.3. *Selection of the Area of the Monoceros SNR*

SNRs radiate both in radio and infrared. Since we are interested in the extinction and dust of SNRs, the dust emission map would be the appropriate indicator of the region of SNR. As dust dominates the infrared emission between $5\mu\text{m}$ and $600\mu\text{m}$ (Draine 2011), we make use of the observation by IRAS at $60\mu\text{m}$ to trace the warm dust towards the line of sight of a $7^\circ \times 7^\circ$ field centered at (Gal: $205^\circ 5', +0^\circ 5'$), almost the very center of the Monoceros SNR (Figure 1). The whole field contains 2,725 stars all picked from our star sample described above, which form a sub-sample to study the extinction and distance of stars and nebulas. We will use it to analyze the uncertainties of the derived distance in Section 3.5.

According to the contour map of the target regions (Figure 1), we determine the bounds of the faint SNR by the 25 MJy/sr contour (the magenta line), while by the 50 MJy/sr contour for the compact region of Rosette Nebula (the cyan line). For NGC 2264, the bound is also defined by the 25 MJy/sr contour (the white line) in order to include as many as possible stars for tracing its extinction. After defining the borders of the nebulas, the 'tracing stars' are extracted from the sub-sample in an irregular polygonal field for Monoceros which basically follows the bound defined by infrared flux, and so is done for the other two nebulas. In order to study the foreground extinction, we additionally select eight rectangular diffuse fields (DFs) around the three nebulas, where no obvious dust emission is visible. The number of selected stars in each field are displayed in Table 2.

3. CALCULATION OF STELLAR EXTINCTION AND DISTANCE

3.1. *Intrinsic color indexes*

We determine stellar intrinsic color indexes between band λ_1 and λ_2 , $C_{\lambda_1\lambda_2}^0$, from their T_{eff} measured by APOGEE or LEGUE. Ducati et al. (2001) suggest that the stars around the blue edge in the $T_{\text{eff}} - C_{\lambda_1\lambda_2}$ diagram have the smallest extinction. For large sky survey projects, such as LEGUE and APOGEE, extinction-free stars are included and appear as the bluest ones in the $T_{\text{eff}} - C_{\lambda_1\lambda_2}$ diagram. That is to say the observed colors of these stars are indeed their intrinsic colors. By fitting $C_{\lambda_1\lambda_2}$ of the chosen extinction-free stars in some temperature intervals, an analytical relation of $C_{\lambda_1\lambda_2}^0$ with T_{eff} can be derived. This method has recently been applied to determining stellar intrinsic colors in infrared (Wang & Jiang 2014; Xue et al. 2016; Jian et al. 2017). Here we adopt the analytical function determined by Xue et al. (2016) to calculate the intrinsic colors, C_{JH}^0 and C_{JKS}^0 , for giants:

$$C_{\text{JH}}^0 = 6.622 \times \exp\left(-\frac{T_{\text{eff}}}{1846\text{K}}\right) + 0.019 \quad (1)$$

$$C_{\text{JKS}}^0 = 20.285 \times \exp\left(-\frac{T_{\text{eff}}}{1214\text{K}}\right) + 0.209 \quad (2)$$

For the dwarf stars which are not studied in [Xue et al. \(2016\)](#), the relation of $C_{\lambda_1\lambda_2}^0$ with T_{eff} is derived in the same way through the selected LAMOST/LEGUE dwarfs. Firstly, the stars are binned according to their T_{eff} with a 50 K step from 4000 K to 7000 K. Then the bluest 5% stars are extracted from each bin and the median value of their colors is taken as the intrinsic color index in each bin. A quadratic function is used to fit the median color indexes of the bluest 5% dwarfs and T_{eff} :

$$C_{\lambda_1\lambda_2}^0 = a_0 + a_1 \times \left(\frac{T_{\text{eff}}}{1000\text{K}} \right) + a_2 \times \left(\frac{T_{\text{eff}}}{1000\text{K}} \right)^2. \quad (3)$$

The result is shown in Figure 2 and the coefficients for C_{JH}^0 and C_{JKs}^0 are listed in Table 3. High consistency is found with the very recent determination of intrinsic colors for dwarfs by [Jian et al. \(2017\)](#). The difference is no larger than 0.05 for C_{JKs}^0 , 0.005 for C_{JH}^0 .

As discussed by [Jian et al. \(2017\)](#), the uncertainty of intrinsic color index comes from a few contributors and can be expressed as:

$$\sigma_{\text{CJA}} = \sqrt{\sigma_{\text{para}}^2 + \sigma_{[\text{Fe}/\text{H}]}^2 + \sigma_{\text{ratio}}^2} \quad (4)$$

where σ_{para} represents the error from the uncertainties of photometry and stellar parameters, and we finally yields 0.002 for dwarfs and 0.003 for giants by a Monte Carlo simulation. The specific technique of the simulation is presented in detail in Section 3.1.1. $\sigma_{[\text{Fe}/\text{H}]}$ refers to the influence of $[\text{Fe}/\text{H}]$, we suggest an error of 0.02 for dwarfs and 0.04 for giants, based on the discussion in Section 3.1.2. σ_{ratio} refers to the error induced from the bluest fraction we adopt to choose extinction-free stars. [Jian et al. \(2017\)](#) discussed different fractions and their effect on the intrinsic colors, and set the error as 0.02.

3.1.1. The Monte Carlo Simulation

Monte Carlo simulation (MCS) is a simple way to estimate the statistical uncertainty caused by the stellar parameter measurement and photometry. Firstly, we assume a Gaussian error distribution on each observed data point in the $T_{\text{eff}} - C_{\lambda_1\lambda_2}$ plane and on the estimated errors in JHK_s magnitude and T_{eff} . The peak value of the distribution is the observed value of each parameter, like colors and T_{eff} , and the Gaussian has a width equals to the estimated error. Then a random data point is sampled for each observed point from two independent Gaussian functions because the colors and T_{eff} are determined independently,

$$f(x; A, \mu, \sigma) = A \exp \left[-\frac{(x - \mu)^2}{2\sigma^2} \right], \quad (5)$$

where x is the color or T_{eff} , μ and σ are correspondingly the observed values and estimated errors, respectively. We subsequently redid the fitting described in Section 3.1 with these randomly sampled points to get new coefficients. LAMOST/LEGUE dwarfs make up the sample set to determine intrinsic colors for dwarfs. Meanwhile, for giants, we still follow the data set and functional form of [Xue et al. \(2016\)](#).

This process is carried out 20,000 times to yield an overall distribution of coefficients, and the standard deviation of the distribution is the uncertainty of coefficients which are listed in Table 3 and 4. Furthermore, the standard deviations of intrinsic colors can also be calculated by these sets

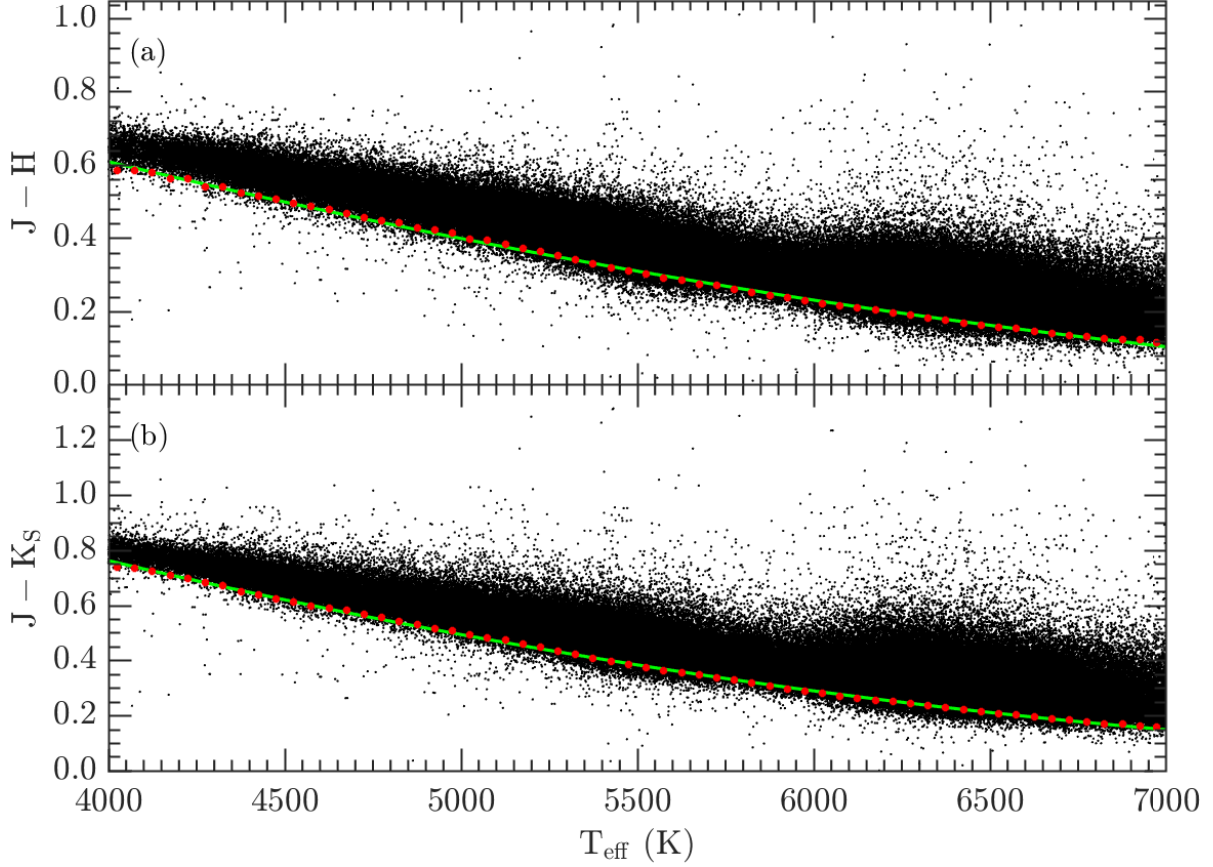


Figure 2. Determination of the relation of the intrinsic colors, C_{JH}^0 and C_{JKs}^0 , with T_{eff} , for dwarfs. The red dots denote the median colors of the 5% bluest stars in each T_{eff} bin and the green lines are the fitting curves.

of coefficients. As the coefficients are correlative with each other, we take some typical temperatures and calculate the intrinsic colors by the MCS result. The errors are derived from the resultant distribution and presented in Figure 3. We can find that the errors are no larger than 0.002 for dwarfs, and no larger than 0.003 for giants. Although $\sigma_{T_{\text{eff}}}$ is on the order of one hundred kelvin, and photometric errors are hundredth magnitude, the statistical method based on the large sample makes these measured and observed uncertainties have very weak influence on the intrinsic colors.

Table 3. The fitting coefficients of intrinsic colors for dwarfs, and their standard errors derived by Monte Carlo simulation.

	a_0	a_1	a_2
C_{JH}^0	1.8568(± 0.0203)	-0.3944(± 0.0072)	0.0206(± 0.0006)
C_{JK}^0	2.4715(± 0.0201)	-0.5550(± 0.0071)	0.0319(± 0.0006)

3.1.2. The Influence of [Fe/H]

Table 4. The same as Table 3, but for giants, with the functional form following [Xue et al. \(2016\)](#): $C_{\lambda_1\lambda_2}^0 = a_0 \times \exp\left(-\frac{T_{\text{eff}}}{a_1}\right) + a_2$.

	a_0	a_1	a_2
C_{JH}^0	$6.622(\pm 1.125)$	$1846(\pm 60)$	$0.019(\pm 0.021)$
C_{JK}^0	$20.285(\pm 2.356)$	$1214(\pm 29)$	$0.209(\pm 0.014)$

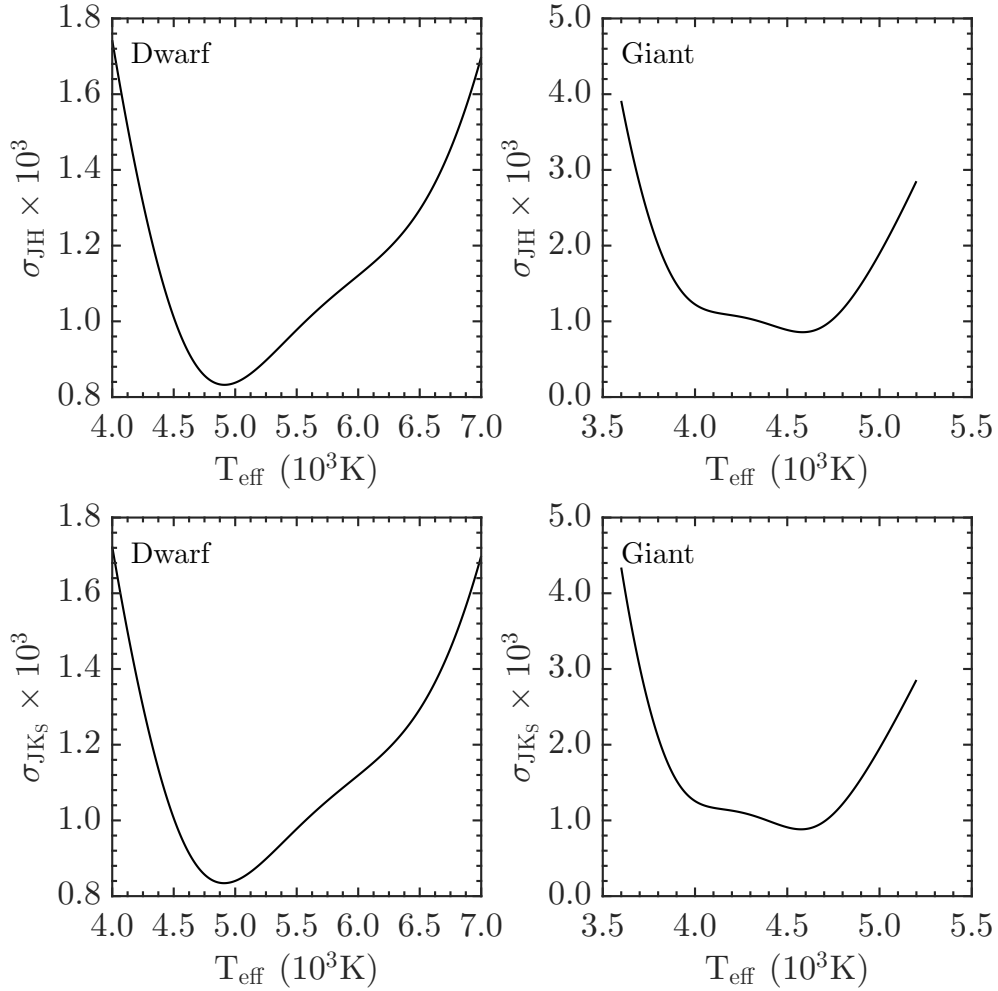


Figure 3. The uncertainties of intrinsic colors caused by the errors of photometry and T_{eff} , derived from the Monte Carlo simulation.

[Jian et al. \(2017\)](#) analyzed the influence of $[\text{Fe}/\text{H}]$ on the infrared intrinsic colors. They found that the difference between metal-normal and metal-poor groups (with a border at $[\text{Fe}/\text{H}] = -0.5$) is a few percent magnitude, no larger than 0.06. For a higher accuracy, dwarfs are further divided into 8 groups from $[\text{Fe}/\text{H}] = -0.5$ to $[\text{Fe}/\text{H}] = 0.5$ with a step of 0.125 dex, and giants are divided into 6 groups from $[\text{Fe}/\text{H}] = -1$ to $[\text{Fe}/\text{H}] = 0.5$ with a step of 0.25 dex. In each $[\text{Fe}/\text{H}]$ bin, C_{JKS}^0

is determined by the method described in Section 3.1. Figure 4 shows the fitting results and the influence of $[\text{Fe}/\text{H}]$ on the intrinsic color.

Metal-rich stars account for a pretty small proportion of both dwarfs and giants, which leads to removing the last group of dwarfs and the abnormal behaviours of the fitting curves (the dashed blue line and solid red line in Figure 4 (left)) The differences for dwarfs are mainly within $[-0.02, 0.02]$, so we take 0.02 as the dispersion of intrinsic colors caused by the variation of metallicity. For giants, the differences are much larger, especially at low T_{eff} . The dispersion rises to 0.04 for $4000 \text{ K} < T_{\text{eff}} < 5200 \text{ K}$. At low T_{eff} , the dispersion increases for both dwarfs and giants, reaching almost 0.1 mag for giants when $T_{\text{eff}} < 4000 \text{ K}$. But it may partly come from the uncertainty of stellar parameters at low T_{eff} in addition to metallicity.

We prefer to taking these uncertainties (0.02 for dwarfs and 0.04 for giants) as a part of the total uncertainty of our intrinsic color model rather than deriving the relation between them. It's because: 1) T_{eff} is the dominating factor for the intrinsic colors while $[\text{Fe}/\text{H}]$ has a much weaker effect in near-infrared; 2) The mean error of $[\text{Fe}/\text{H}]$ for dwarfs is about 0.14 dex, which constrain the bin box size; 3) There are not enough metal-poor and -rich stars to complete the fitting.

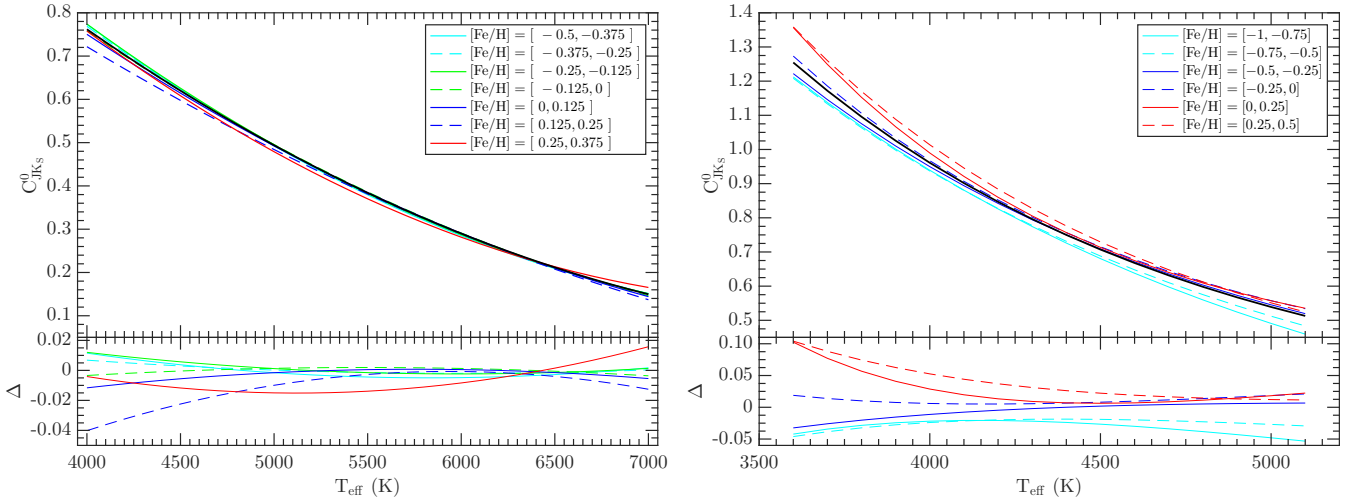


Figure 4. The influence of $[\text{Fe}/\text{H}]$ on intrinsic colors of dwarfs (left) and giants (right). In the upper panels, the intrinsic colors derived from different $[\text{Fe}/\text{H}]$ bins are present in different colors and linestyles, the black solid line presents the result derived using the whole $[\text{Fe}/\text{H}]$ samples. In the lower panels, colored lines show the differences between the corresponding bins and the whole samples' result.

3.2. A_{K_S} : Interstellar Extinction in the K_S Band

The color excess is calculated straightforward after subtracting the intrinsic one from the observed. The extinction in the K_S -band, A_{K_S} , must also be derived in order to calculate stellar distance. The conversion from color excess, $E_{J_{K_S}}$, to the extinction, A_{K_S} , depends on extinction law in principle. The near-infrared extinction law is commonly expressed by a power law $A_\lambda \propto \lambda^{-\alpha}$. The universality of the near-infrared extinction law (Wang & Jiang 2014) brings the convenience to convert the color excess into the absolute extinction in the K_S -band. Based on the all-sky survey data, Xue et al. (2016) derived an average $E_{JH}/E_{JK_S} = 0.652$, which corresponds $\alpha = 1.79$ and $A_J/A_{K_S} = 2.72$. This conversion factor is adopted to convert E_{JK_S} to A_{K_S} . The uncertainty of A_{K_S} is then

$$\sigma_{A_{K_S}} = \sigma_{E_{JK_S}}/1.72, \quad (6)$$

and

$$\sigma_{E_{JK_S}} = \sqrt{\sigma_J^2 + \sigma_{K_S}^2 + \sigma_{(J-K_S)_0}^2}, \quad (7)$$

where $\sigma_{(J-K_S)_0}$ is the uncertainty of intrinsic color discussed in Section 3.1, and σ_J and σ_{K_S} are the observed errors.

3.3. The Absolute Magnitude

We use the *PAdova and TRieste Stellar Evolution Code* (PARSEC) to compute stellar absolute magnitudes. The new PARSEC is an updating of the Padova database which can calculate sets of stellar evolution tracks (Bressan et al. 2012). We obtain stellar evolution tracks calculated by PARSEC through CMD 3.0. CMD 3.0¹ is a set of routines that provide interpolated isochrones in a grid, together with stellar parameters and absolute magnitudes transformed into various photometric systems (see Girardi et al. 2002, 2004). The isochrone grids we use in this work have a metallicity step of 0.001 dex between $0.005 < Z < 0.048$ and an age spacing of $\Delta \log(t) = 0.05$ Gyr.

For each star, we select the isochrone closest in metallicity and then the K_S -band absolute magnitude, M_{K_S} , is calculated by a two-dimensional cubic interpolation with neighboring grid points in the corresponding T_{eff} and $\log g$ plane, rather than directly adopting the closest point. In this way, the accuracy of M_{K_S} is improved in the low density area. Additionally, for a query star with a specific type, the grid points are filtrated by the parameter ‘stage’, which indicates the stellar evolution phase, to alleviate the contamination of other type stars. If a star lies out of the network constructed by the theoretical isochrones, the grid points will focus on one side of it and extrapolation is needed to calculate M_{K_S} . In such case, no calculation is done for this star because errors and uncertainties would be unpredictable.

The typical uncertainty of M_{K_S} calculated by the PARSEC code is composed of two parts:

$$\sigma_{\text{total}} = \sqrt{\sigma_{\text{para}}^2 + \sigma_{\text{inter}}^2} \quad (8)$$

where σ_{para} is the contribution by stellar parameters’ error, and σ_{inter} is caused by the interpolation.

Schultheis et al. (2014) present a simple method to estimate σ_{para} . For each star, a new set of stellar parameters is constructed by adding the errors, i.e. $T_{\text{eff}} \pm \Delta T_{\text{eff}}$, $\log g \pm \Delta \log g$, and $[\text{Fe}/\text{H}] \pm \Delta_{[\text{Fe}/\text{H}]}$, which is taken as a new input to calculate the lower and upper limits of M_{K_S} . Consequently, the range of M_{K_S} is calculated and the half difference of the lower and upper limits with M_{K_S} is regarded as the uncertainty. This method is applied to the 2,725 sub-sample stars mentioned in Section 2.3, and M_{K_S} is successfully derived for 2,218 stars. While the remainder lie out of the theoretical network, so as mentioned above, they are beyond calculation and dropped. Figure 5 presents the variation of the error $\sigma_{M_{K_S}}$ with M_{K_S} . The sample stars gather into three distinct parts, associating with their data sources and stellar types. There is no correlation between $\sigma_{M_{K_S}}$ and M_{K_S} , while stars observed by LAMOST generally have significantly higher $\sigma_{M_{K_S}}$ than APOGEE. This can be understood by the larger error in stellar parameters of the LAMOST survey, in particular the apparently lower quality in $\log g$ and $[\text{Fe}/\text{H}]$ than the APOGEE survey.

¹ CMD is being extended/updated every few months, and the last version is always linked in <http://stev.oapd.inaf.it/cmd>

For a sample star, we take the interpolated error of its closest grid point as its σ_{inter} . The interpolated error equals the difference between intrinsic value of M_{K_S} of the grid point and the interpolated value calculated by adjacent ones with $\Delta T_{\text{eff}} < 200$ K and $\Delta \log g < 0.2$ dex. Mostly, σ_{inter} is smaller than 0.05 and negligible in comparison with σ_{para} .

The errors we discuss above do not include the contribution of the PARSEC model itself. [Schultheis et al. \(2014\)](#) discussed the differences between the PARSEC isochrones and the Basel3.1 model library ([Lejeune et al. 1997](#)). They suggest that systematic differences exist in calculating the magnitudes and distances between the two libraries, significant for cool, metal-poor M giants. Fortunately, we only take use of the G- and K-type giants, which may not be seriously affected.

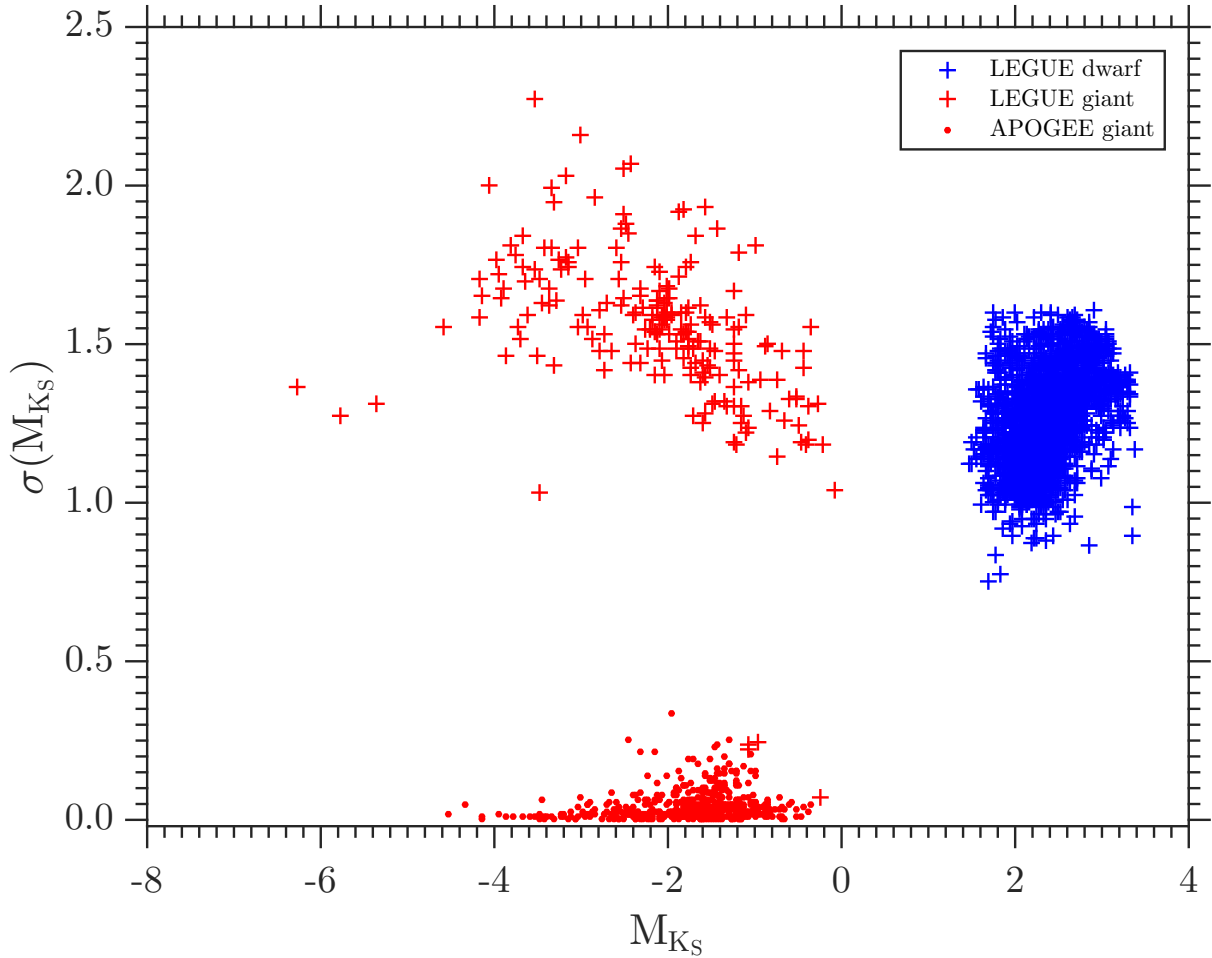


Figure 5. Uncertainty of M_{K_S} caused by the errors of stellar parameters. The sample stars gather into three distinct parts: blue and red crosses are dwarfs and giants from LEGUE, respectively, and red dots are giants from APOGEE.

3.4. The Stellar Distance

The distance of individual star is calculated by

$$D(\text{pc}) = 10^{[(m_{K_S} + 5 - M_{K_S} - A_{K_S})/5]}, \quad (9)$$

where m_{K_S} , M_{K_S} , and A_{K_S} are the apparent magnitude, absolute magnitude and extinction magnitude in K_S -band, respectively. According to the error analysis above, the relative uncertainty of distance is:

$$\sigma_D/D = 0.46 (\sigma_{m_{K_S}} + \sigma_{M_{K_S}} + \sigma_{A_{K_S}}). \quad (10)$$

For the 2,218 sample stars with M_{K_S} available, the relative error of distance is shown in Figure 6. As predictable, the errors for the LAMOST stars (both dwarfs and giants) are significant, mostly above 50% from the uncertainty of derived absolute magnitude M_{K_S} . On the other hand, the APOGEE giants appear with much smaller uncertainty, mostly around 2 – 5% and never superseding 20%, even when the distance reaches 8 kpc. Consequently, the LAMOST dwarfs may be problematic in describing the run of reddening towards the targets. Meanwhile, as most dwarfs are located within 1 kpc, this effect is weak for the Monoceros and Rosette nebulas, while non-negligible for the closer object NGC 2264.

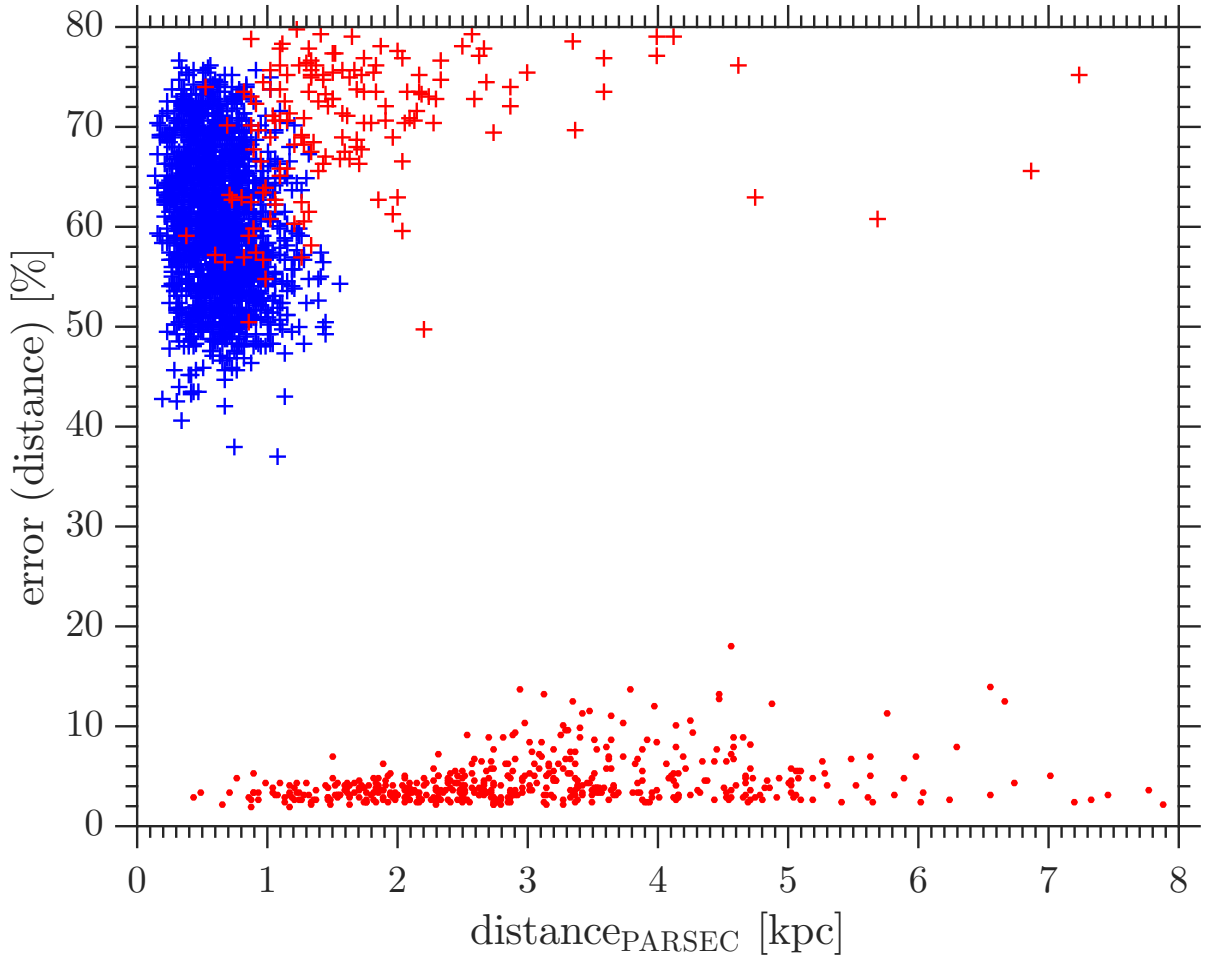


Figure 6. The relative distance error. The distance errors account the contributions both of the stellar parameters and the interpolation. The red dots are APOGEE giants, the blue and red crosses are LEGUE dwarfs and giants, respectively.

3.5. The Distance from Parallax

Recently, the first version of data from the European Space Agency (ESA)’s *Gaia* mission is released (Gaia Collaboration et al. 2016a,b). It contains the *Tycho – Gaia Astrometric Solution* (TGAS, Michalik et al. 2015) catalog, which provides stellar parallaxes for about 2 million stars. The distances computed by parallaxes are independent of stellar parameters and stellar model, which is a very good examination of the distances derived by our method.

With the requirement of the error of parallactic distance less than 20%, matching TGAS with LEGUE and APOGEE results in 38,222 dwarfs and 1,468 giants (996 from LEGUE, 472 from APOGEE). Among them, there are 143 dwarfs and 4 giants in our target region.

Figure 7 compares the distance differences, where the dash lines delineate the 20% borders. It can be seen that most dwarfs have the differences less than 20%, comparable to the error of TGAS. The mean difference is close to zero, and a systematical deviation occurs when $d > 0.6$ kpc in the way the model distance is larger than the parallactic distance. Dwarfs in our target regions (green crosses) show a similar tendency. For giants in the right panel of Figure 7, the difference is on the same order as the dwarfs, and has no clear difference between the LEGUE and APOGEE data. Recalling that the estimated errors of distances for the LEGUE stars are generally larger than 50% in Section 3.4, the distance errors must be greatly overrated as a result of the overestimation of $\Delta \log g$ derived from the LAMOST spectra. There is a tendency that the model distance becomes larger than the parallactic linearly with the distance when it is greater than 0.6 kpc. This tendency is visible for both dwarfs and giants, while more significant for giants at larger distance. That means our method tends to yield larger distance for relatively distant stars in comparison with the TGAS data. This may lead to the overestimation of distances. On the other hand, Davies et al. (2017) found that the TGAS distance showed systematical deviation to larger distance at $d > 0.5$ kpc for the Kepler field of view. Stassun & Torres (2016) also reported that the GAIA distance is offset to large. The GAIA distance, when > 0.5 kpc, needs better calibration. It’s puzzling that the GAIA distance is smaller than our model distance when > 0.6 kpc. If the problem lies in the model distance, the systematic deviation should also occur to the small distance stars while it does not.

4. THE DISTANCE AND EXTINCTION OF THE MONOCEROS SNR

The distance of the Monoceros SNR can now be derived based on the extinction and distances of individual stars in this sightline. The pre-assumption is that interstellar extinction increases monotonically with distance at a given sightline, which is very reasonable as the extinction is an integral parameter along the sightline. There will be a sharp increase at the position of the Monoceros SNR because of its higher dust density than the foreground diffuse ISM. The position of the sharp increase will tell the distance of the nebula.

4.1. The foreground extinction

Because extinction is an integral effect, the foreground extinction must be subtracted in order to measure the extinction produced by the SNR alone. For a precise determination of the foreground extinction, 8 DFs are selected as described in Section 2.3. The change of extinction with distance for the stars in these 8 DFs are shown in Figure 8 and a linear fitting is performed for simplicity, alongwith a 3σ uncertainty region. It can be seen that the slopes agree with each other for DF1, DF3, and DF4 with a value of about 0.02 mag per kpc in A_{K_S} , as well as for DF2 and DF8 with a slightly smaller value of about 0.01 mag per kpc. Meanwhile the DF5 to DF7 variations have a much

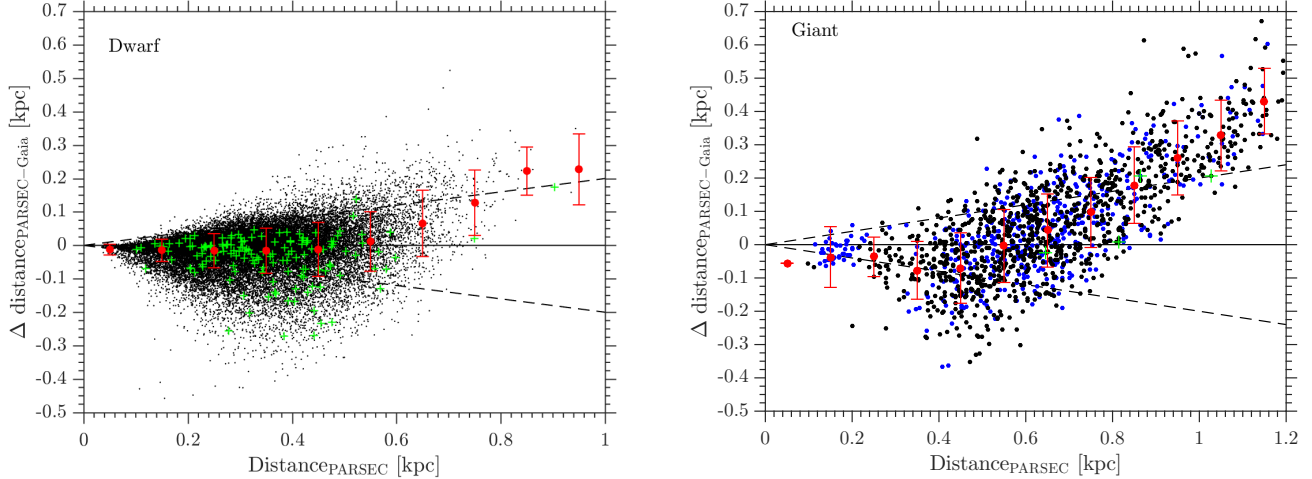


Figure 7. Our model distances compared to those obtained using the TGAS stellar parallaxes for dwarfs (left) and giants (right). In both panels: the green crosses are the sample stars extracted from the $7^\circ \times 7^\circ$ target region, and the red dots are the mean values of differences in each distance bins with a bin size of 0.1 kpc. The dash lines indicate the 20% borders. On the right panel: blue dots from APOGEE, and black dots from LEGUE.

higher slope, being about 0.05 mag per kpc. This is caused by the Galactic latitude as DF1–DF4 and DF8 have slightly higher latitude, while the variation of slopes between them from 0.009 to 0.025 is mainly due to the local environment. Considering the average rate of interstellar extinction in the V –band is usually taken to be 0.7 – 1.0 mag/kpc (Gottlieb & Upson 1969; Milne & Aller 1980), and the K_S –band extinction is about 10% of the V –band, the derived foreground extinction rate does mean a diffuse foreground.

For the foreground extinction of the Monoceros SNR, a $1.5^\circ \times 2.0^\circ$ reference region (marked by black dot dash lines in Figure 1) is chosen with the center at $(l, b) = (208^\circ.25, +0^\circ.5)$ including DF5 and DF6, for its similar latitude (Figure 9). This foreground will also be applied to the Rosette Nebula and NGC 2264. The extinction of a star, within the uncertainty (3σ) of linear fitting, is mainly produced by the diffuse ISM rather than by the nebula. We must take this part of extinction out to study the extinction and near-infrared color excess ratios for the nebulas in Section 5.

4.2. The Nebular Distance and Extinction

The change of stellar extinction A_{K_S} with distance D , is shown in Figures 10–12 for the three selected nebular regions. To be reasonable, only stars with $E_{JH} > 0$ and $E_{JK_S} > 0$ are regarded as the correct indicators. For a better accuracy, $\sigma_D/D < 100\%$ is also required. For the Monoceros SNR, it can be seen that there are three stars (located in the green box in Figure 10) whose extinctions clearly jump around 2.0 kpc. In order of distance, they are (1) $A_{K_S} = 0.26$ at 1.98 kpc, (2) $A_{K_S} = 0.36$ at 2.31 kpc, and (3) $A_{K_S} = 0.35$ at 2.32 kpc. As the nebular extinction shows up only when the star lies behind, the stellar distance should be the upper limit of the Monoceros SNR. The three stars thus indicate the upper limit of the distance. We tend to believe the closest distance, i.e. 1.98 kpc is the nebular distance and the other two stars are behind the SNR. The dispersion of the extinction is mainly caused by the inhomogeneity of the SNR. On the other hand, the tracers are located densely around 2.0 kpc, this distance should be very close to the position of the SNR nebula. In addition,

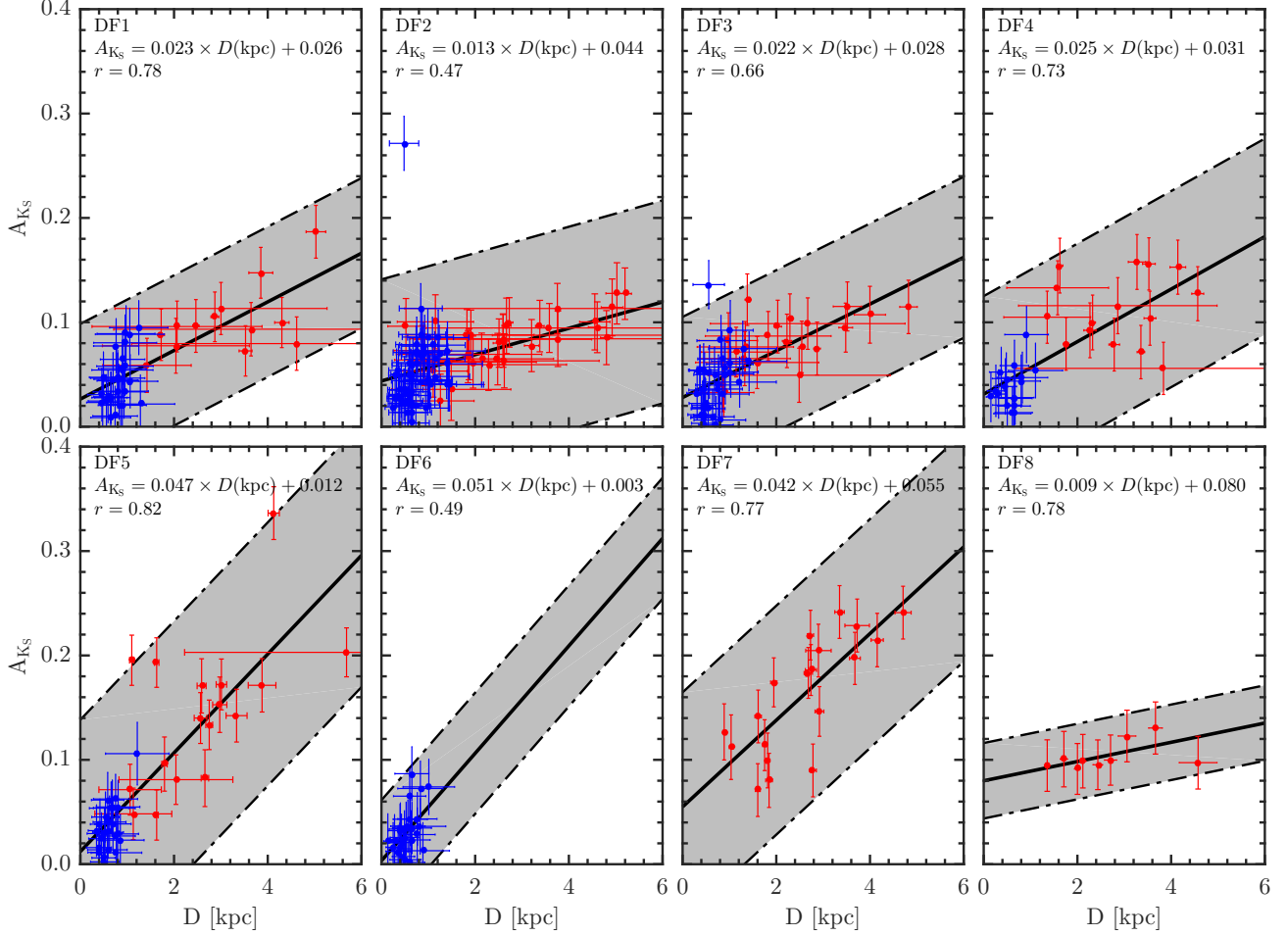


Figure 8. The change of extinction with distance for stars in the 8 DFs. The blue dots are dwarfs and the red ones are giants. The fitting results are also listed in sub-panels, along with the correlation coefficient (r) and the name of each DF. The grey shaded region in each sub-panels encloses the 3σ uncertainty.

there is no apparent increase of extinction up to at least 1.9 kpc. Therefore, the distance of the Monoceros Nebula is between 1.90 – 1.98 kpc.

The extinction of the Rosette Nebula, $\Delta A_{K_S} \approx 0.5$ mag, is twice that of the Monoceros SNR. From Figure 11, the distance of Rosette can be determined to be less than 1.55 kpc as a star at 1.55 kpc has an apparent increase in A_{K_S} , with $\Delta A_{K_S} > 0.5$ mag, which is followed by several stars (in the green box in Figure 11) with similarly steeply rising extinction. NGC 2264 has an extinction jump of $\Delta A_{K_S} \approx 0.25$ mag at 1.20 ± 0.03 kpc (Figure 12), which sets the distance at 1.20 kpc. However, there is one dwarf (blue cross in Figure 12) with a distance of 0.35 kpc and $A_{K_S} = 0.24$ mag, obviously larger than other dwarfs nearby. We suspect this star is mis-classified as a dwarf while it may be a giant star at much larger distance. No cloud is claimed at this distance at this sightline. In addition, no neighbour stars follow the tendency, and this distance is too much smaller than previous results. Instead, there are quite some stars showing up above the foreground and background extinction after the star at 1.20 kpc. So 1.20 kpc should be the distance of NGC 2264.

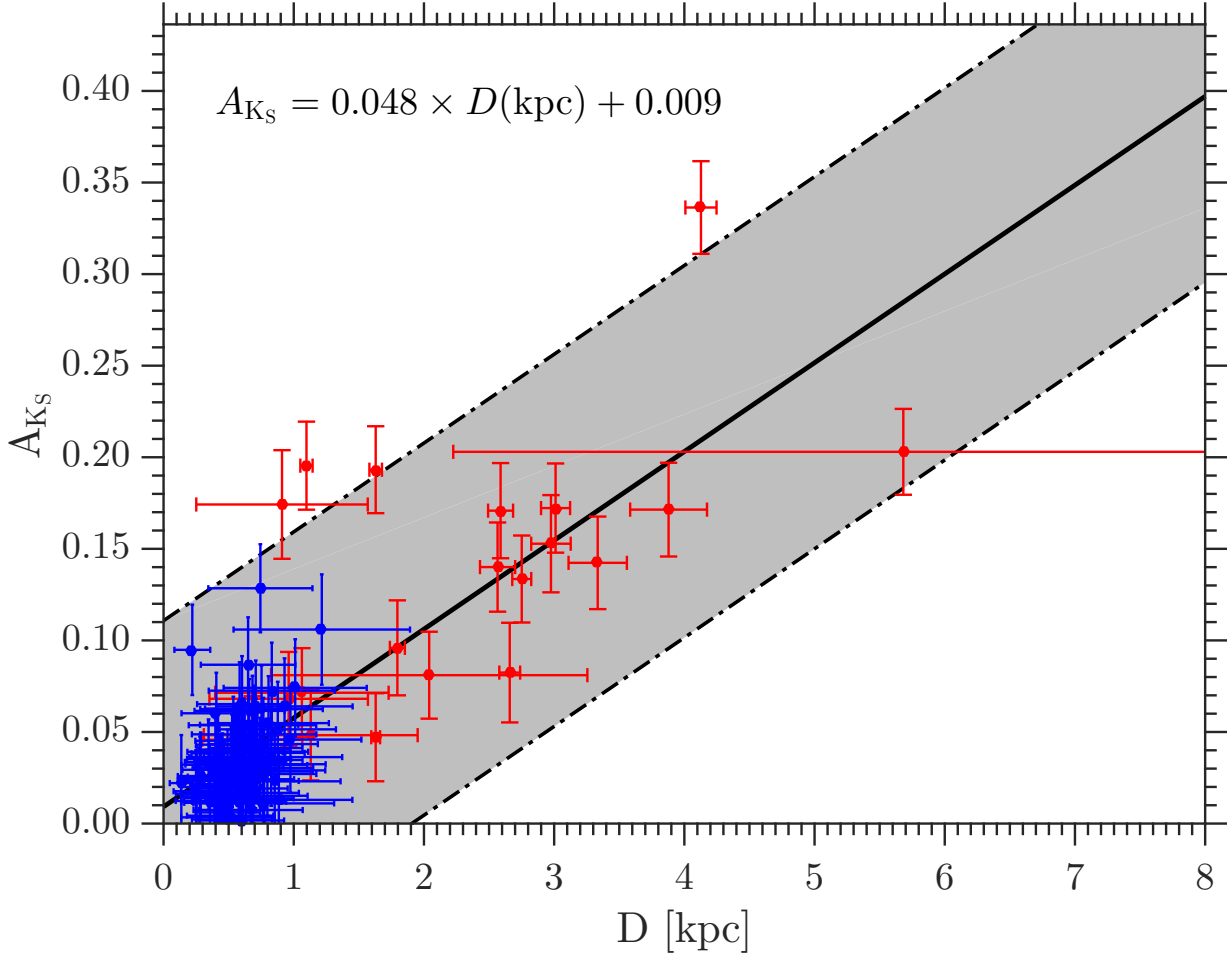


Figure 9. The run of reddening of stars in the reference region, that will be used to estimate the extinction contributed by ISD for the Monoceros SNR as well as the Rosette Nebula and NGC 2264. The blue dots are dwarfs and the red ones are giants. The grey shaded region encloses the 3σ uncertainty.

Table 5 compares the derived distances to the three nebulae with previous studies. The distance of the Monoceros SNR is 1.98 kpc, appearing larger than previous value of ~ 1.6 kpc. Meanwhile, the distance of the Rosette Nebula, 1.55 kpc, coincides with previous results. According to our new determinations of the distances, there should be no interaction between these two nebulae as their distance difference is about 0.4 kpc. The distance to NGC 2264, 1.2 kpc, is larger than previous results, but quite close to the result of [Morgan et al. \(1965\)](#), 0.95 kpc. Overall, the positional relation of the three nebulae is consistent with [Davies et al. \(1978\)](#), i.e. the Monoceros Nebula is the furthest, NGC 2264 the closest and the Rosette Nebula in-between.

The location of the nebular tracers is shown in Figure 13 (a)–(c). There are no stars in the highest $60\mu\text{m}$ emission regions for all the three nebulae very possibly because of too high extinction in comparison with the depth of observation. The tracers mainly distribute near the southern edge of the Monoceros SNR, while the foreground stars with low extinction spread in a wide distance range. No extinction jump is found for these foreground stars in Figure 10, which indicates that the sharp increase in the extinction at 1.90 – 1.98 kpc can only be attributed to the SNR. Although tracers of

Table 5. The nebular distances (in kpc) compared with previous works.

	Monoceros SNR	Rosette Nebula	NGC 2264
This work (upper limit)	1.98	1.55	1.2
Johnson (1962)	-	1.66	-
Becker & Fenkart (1963)	-	2.2	0.715
Morgan et al. (1965)	-	1.7	0.95
Davies et al. (1978)	1.6 ± 0.3	1.6	0.8
Graham et al. (1982)	1.6	-	-
Leahy et al. (1986)	1.5	-	-

the Rosette Nebula are more scattering, the crucial ones still have nearby foreground stars to ensure the distance estimation. As for NGC 2264, with fewer stars, it is hard to exclude the existence of a foreground cloud. But NGC 2264 itself contains a massive dark cloud and the previous work implies a nearest distance of 0.8 kpc, so the possibility is low for a comparable dust cloud in a nearby region.

The nebular dust not only causes extinction to the background stars, but also emits infrared radiation, thus a correlation between the nebular extinction and infrared emission is expected. Figure 13 compares the extinction of stars behind the nebulas and the infrared flux of the nearest pixel as per the IRAS 60 μm (middle panels) and 100 μm (right panels) image, respectively. We made no intention to subtract the background emission from the infrared images because it would be non-uniform for a large extended nebula, such as Monoceros, and consequently hard to model. No correlation is found between the extinction and the 60 μm emission or the 100 μm emission. Although both the extinction and emission is proportional to dust mass, the emission depends sensitively on dust temperature. The 60 μm and 100 μm emission is dominated by warm dust that makes up only a small fraction of the total dust in SNRs (see the dust mass estimation of [Gomez et al. \(2012\)](#) and [De Looze et al. \(2017\)](#)). It also implies that the warm and cold dust do not spatially coincide completely, which is suggested by the dust map of [De Looze et al. \(2017\)](#). A check of the dust emission at longer wavelength may reveal whether the excess extinction is due to the nebular dust. Fortunately, the eastern part of the Rosette Nebula was observed by the Herschel Space Observatory (HSO; [Pilbratt et al. 2010](#)), with its Spectral and Photometric Imaging Receiver (SPIRE; [Griffin et al. 2010](#)) at 250, 350, and 500 μm . We obtained the reduced SPIRE data through the Herschel Interactive Processing Environment (HIPE; [Ott 2010](#)). Figure 14(a) shows the Herschel 500 μm image of the Rosette Nebula together with the sample stars and the nebula border. Most tracing stars are located in the region with the intensity of 30 – 50 MJy/sr, while the dense region is not covered again due to its severe extinction. The distances of individual stars and background emission have much smaller influence at far-infrared that is dominated by the nebular cold dust. It can be seen that there exists tight linear relations of nebular stellar extinction, A_{K_S} , with the dust emission at 250, 350, and 500 μm , respectively (Figure 14(b)), which yields the linear correlation coefficient greater than 0.96. This result shows that the extinction-producing dust is identical to the far-infrared emission dust.

5. THE NEAR-INFRARED EXTINCTION LAW

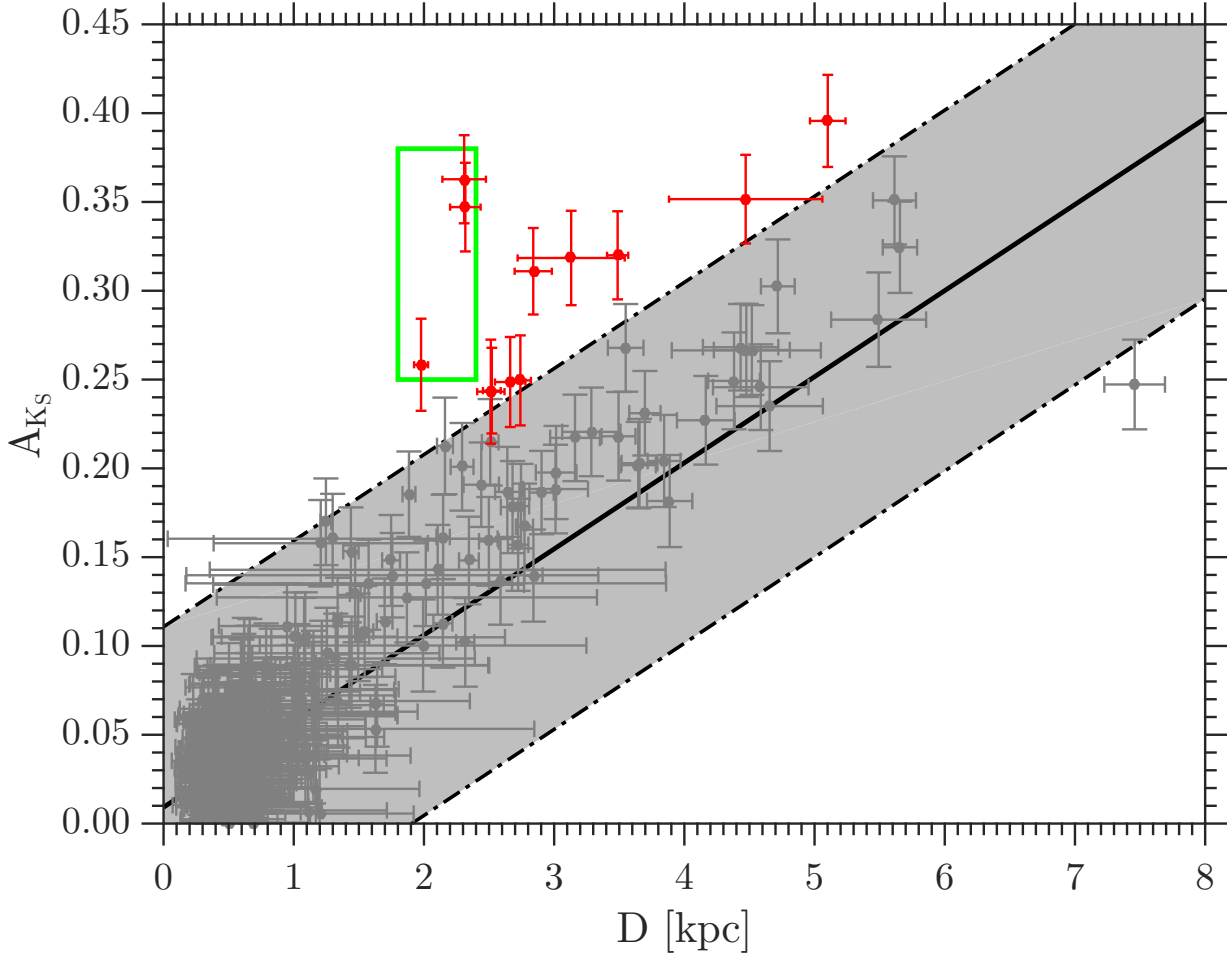


Figure 10. A_{K_S} vs. D for the Monoceros SNR. The background extinction profile and the grey shaded region derived from the reference region are the same as Figure 9. The red dots are giants which are mainly obscured by dust from SNR, while stars in or below the uncertainty region are marked by grey dots. The extinction jump can be seen at 1.98 kpc with $\Delta A_{K_S} \approx 0.15$ traced by three stars in the green box.

Although the near-infrared extinction law takes the form of a power law, the power index α is very sensitive to the adopted wavelengths of the JHK_S -bands. So the color excess ratio, E_{JH}/E_{JK_S} , is a more stable and reliable description of the near-infrared extinction law. Wang & Jiang (2014) and Xue et al. (2016) have already derived the mean E_{JH}/E_{JK_S} of the Milky Way, which are 0.64 and 0.652 respectively and consistent with each other, and the result by Xue et al. (2016) is more preferable for their better determination of the intrinsic color indexes.

Stars behind the nebula are obscured by dust both from the nebula and the diffuse foreground ISD. But the nebula is inhomogeneous, they experience different extent of extinction by the nebula. The extinction by the nebula is calculated by subtracting the interstellar foreground extinction. With the nebular distance derived above, the stars further than this distance are chosen to study the extinction law of the nebula. More over, only the stars with apparent extinction by the nebula are taken as the tracers. In Figure 10, the red dots with errorbars denote the extinction tracers that lie above the 3-sigma level of the background extinction and are used as the tracer stars of the nebular extinction.

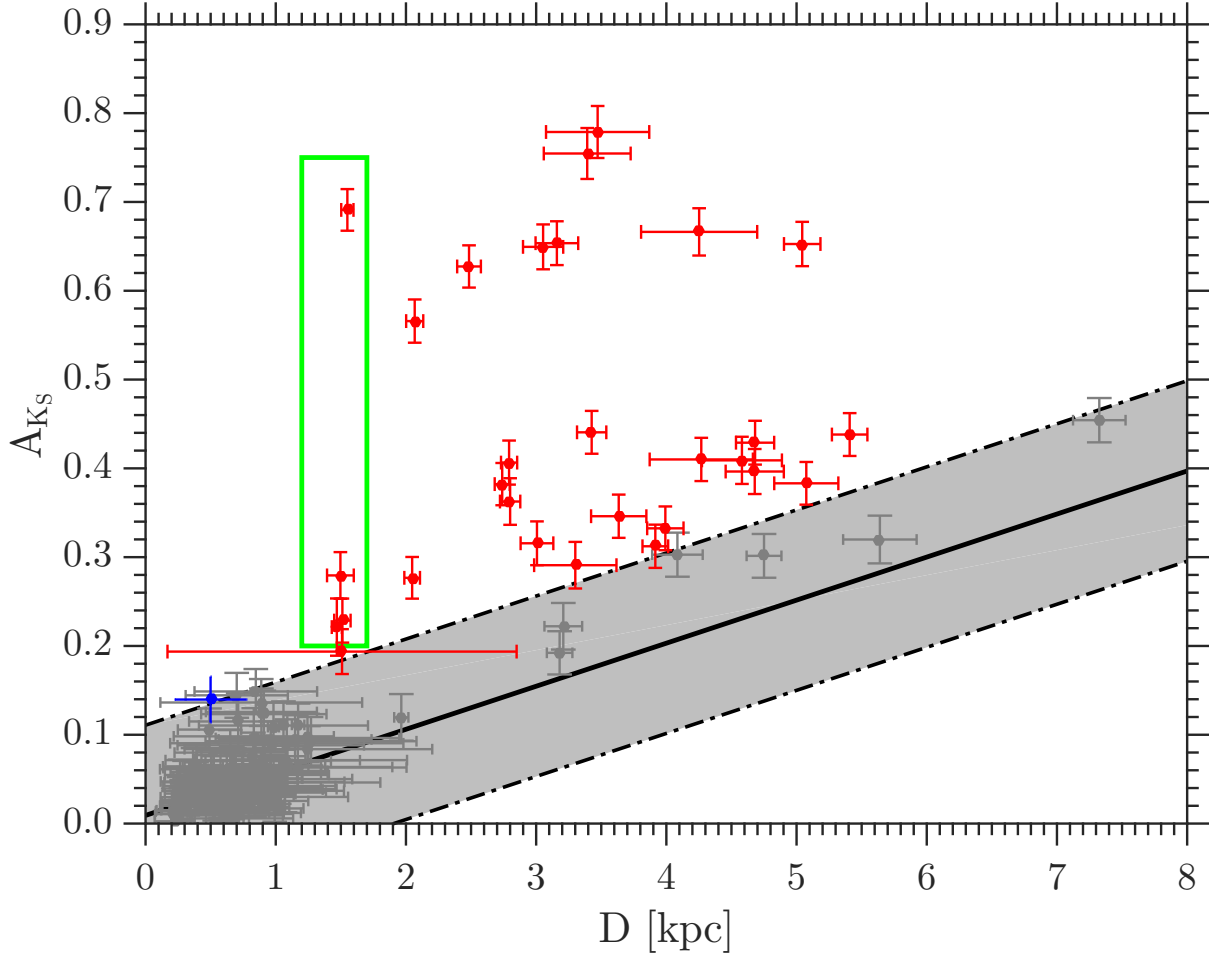


Figure 11. The same as Figure 10, but for the Rosette Nebula. The jump of A_{K_S} can be clearly seen at 1.55 kpc, followed by several high-extinction stars in the green box. The blue point represents a dwarf above the uncertainty region.

The same is for the Rosette nebula and NGC 2264, as shown in Figures 11 and 12. After subtracting the contribution by the background ISM, the color excess ratio, E_{JH}/E_{JK_S} , is derived by a linear fitting between E_{JH} and E_{JK_S} as shown in Figures 15 and in Table 6.

The color excess ratio E_{JH}/E_{JK_S} is 0.657 ± 0.056 for the Monoceros SNR, 0.658 ± 0.018 for the Rosette nebula, which agree with each other, and also with 0.652 by Xue et al. (2016). As Monoceros is an old faint SNR, E_{JH} and E_{JK_S} span a narrow range, which leads to a relatively large uncertainty (0.056) and low correlation coefficient ($r = 0.89$). NGC 2264 has a smaller ratio, $E_{JH}/E_{JK_S} = 0.617$, but with an error of 0.061, it is still consistent with the mean value 0.652. Wang & Jiang (2014) suggest that the near-infrared extinction law is universal based on the fact that there is no visible change of E_{JH}/E_{JK_S} with E_{JK_S} in the range [0.3, 4.0]. The Monoceros SNR shows no significant difference in the near-infrared extinction law from the mean law of the Milky Way, which conforms the universality of the near-infrared extinction law. However, the supernova explosion is a very violent event that releases numerous high energy particles and photons which can destroy the surrounding dust grains. Moreover, the supernova ejecta produce dust grains that may differ from the dust in

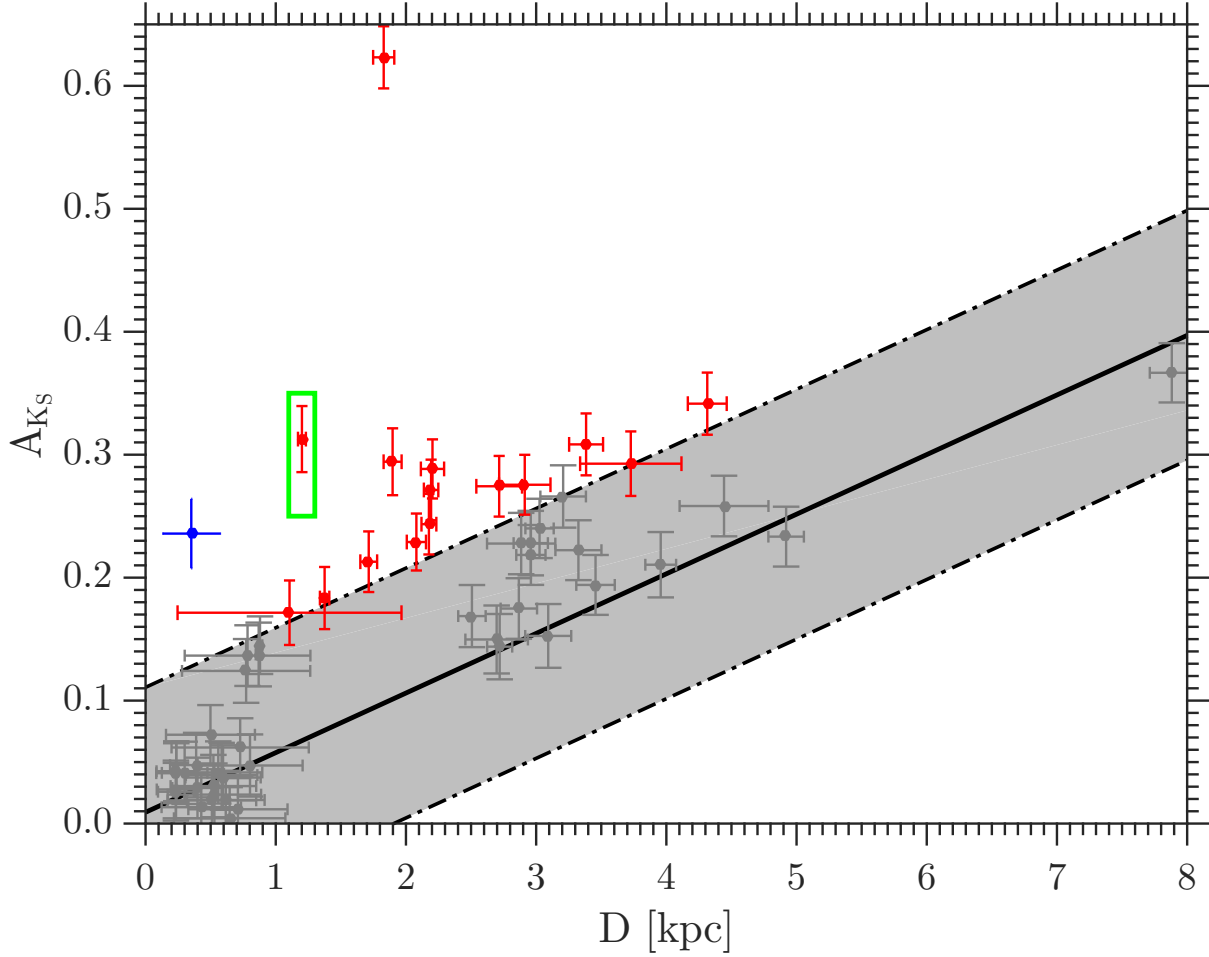


Figure 12. The same as Figure 10, but for NGC 2264.

Table 6. Color excess ratio $E_{\text{JH}}/E_{\text{JKs}}$ of the three nebulae.

	Monoceros SNR	Rosette Nebula	NGC 2264	Xue et al. (2016)
$E_{\text{JH}}/E_{\text{JKs}}$	0.657	0.658	0.617	0.652

the diffuse medium. In principle, the properties of the SN dust are expected to differ so is the extinction law. The highly consistency of the near-infrared extinction law of the two environments does not necessarily mean the SN dust is the same as others or the SN explosion has no effect on the surrounding dust grains. One possibility is that the Monoceros SNR is so old (10^5 yr) that the dust observed is almost the normal ISD with little affected by the SN explosion. The other possibility is that the near-infrared bands cannot trace the difference of the dust. The other bands, in particular the visual and UV bands, may better reflect the difference of the dust.

6. DUST MASS OF THE MONOCEROS SNR

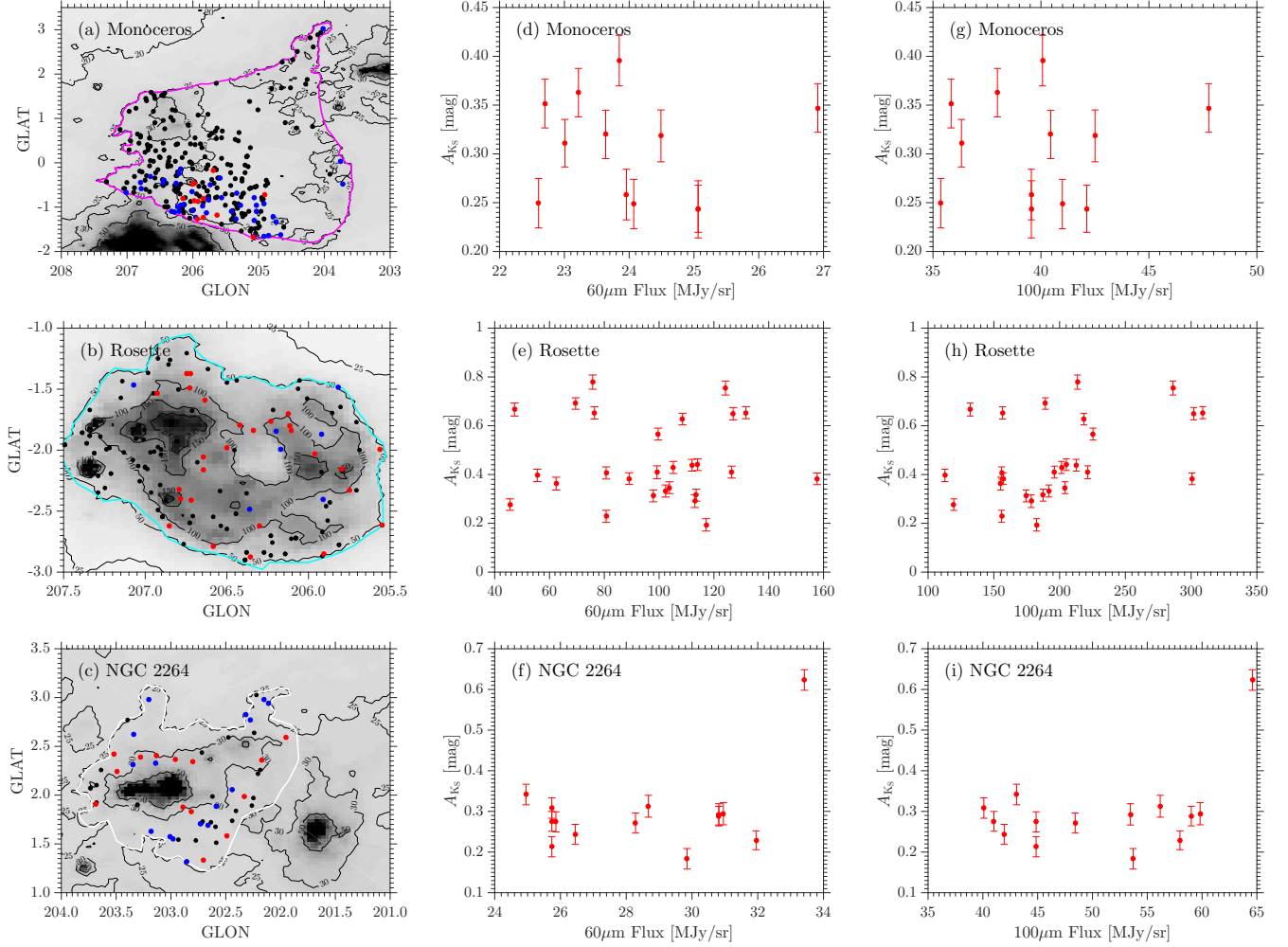


Figure 13. Left panels: The distribution of sample stars. The red dots are the tracing stars, the black ones are the foreground stars, and the blue ones are the stars behind the nebulae which are mainly obscured by the interstellar dust. The contours and nebular borders are the same as Figure 1. Middle and right panels: The relationship between the extinction, A_{K_s} , and the 60 and 100 μm flux from IRAS for the three nebulae, respectively.

In principle, the dust mass of the Monoceros SNR can be derived from its extinction because the extinction is proportional to the dust column density. A precise determination of the dust mass needs the information of the extinction at all wavelengths from which the dust property can be precisely constrained. Nevertheless, a rough estimation of the dust mass can still be derived with the extinction known only in the near-infrared if an extinction law is assumed.

Adopting the WD01 (Weingartner & Draine 2001) dust model for the Galactic interstellar extinction law ($R_V = 3.1$), the mass extinction coefficient for the V -band, $K_{\text{ext},V} = A_V / \Sigma_{\text{dust}}$ is

$$K_{\text{ext},V} = 2.8 \times 10^4 \text{ mag cm}^2 \text{ g}^{-1}. \quad (11)$$

With a surface mass density $\Sigma_{\text{dust}} = A_V / K_{\text{ext},V}$, the dust mass is then

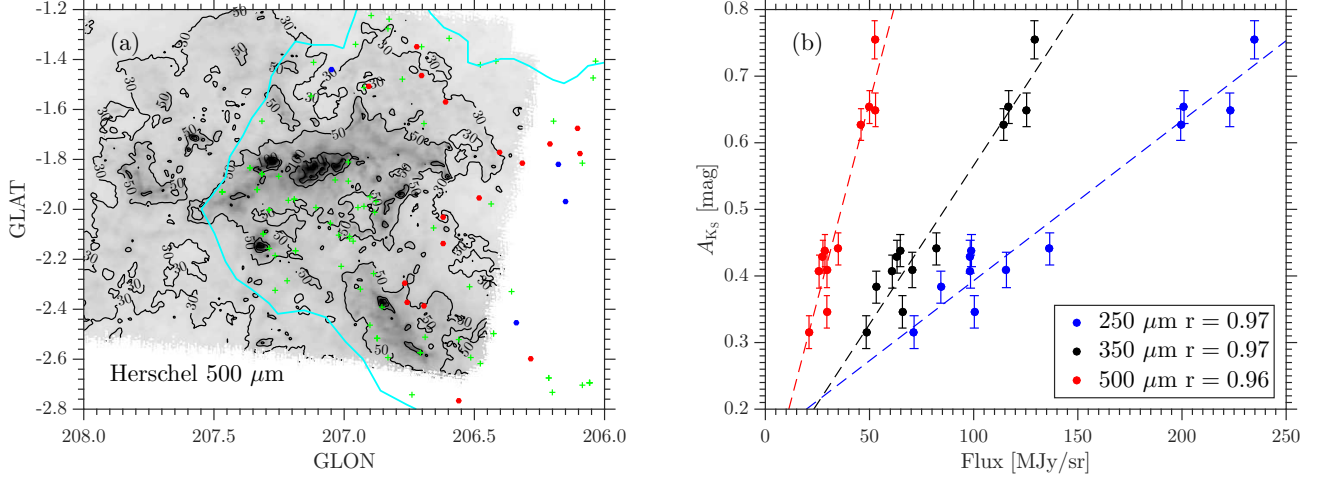


Figure 14. Left: The SPIRE 500 μm image of part of the Rosette Nebula with our sample stars in this sightline and the nebular border (the cyan profile). The green crosses are the foreground stars, and the red and black dots are the same as in Figure 13. Right: The linear relationships between the extinction A_{K_S} and the infrared emission intensity of the Rosette Nebula at 250, 350, and 500 μm , respectively. The correlation coefficients (r) are shown in the legend box.

$$\begin{aligned}
 M_{\text{dust}} &= \Sigma_{\text{dust}} \times A_{\text{eff}} \\
 &= \frac{A_V}{K_{\text{ext},V}} \times A_{\text{eff}},
 \end{aligned} \tag{12}$$

where A_{eff} is the effective surface area.

As a test of this method, we firstly apply it to the SN dust in the Crab Nebula which appears to be a 4.0×2.9 pc ellipsoid (Hester 2008). Owen & Barlow (2015) presented a detailed description of the nebular geometry. To calculate A_{eff} , we follow the dust distribution of their favored models (V and VI): a clumped shell starts at inner axis diameters of 2.3×1.7 pc, and extends to the 4.0×2.9 pc outer boundaries, with a volume filling factor (F_{fil}) of 0.10. If we adopt $A_V = 1.6 \pm 0.2$ mag derived by Miller (1973), the resultant dust mass is $0.658 \pm 0.082 M_{\odot}$ (the uncertainty is simply derived by using $\Delta A_V = 0.2$). This value is in agreement with that by Owen & Barlow (2015) who yielded a result of $0.11 - 0.13 M_{\odot}$ of amorphous carbon and $0.39 - 0.47 M_{\odot}$ of silicate from the infrared emission by using mixed dust chemistry model. However, assuming a single dust species of carbon grains, Gomez et al. (2012) derived warmer (64 ± 4 K) and cooler (34 ± 2 K) components of 0.006 ± 0.02 and $0.11 \pm 0.02 M_{\odot}$, respectively, and Owen & Barlow (2015) derived $0.18 - 0.27 M_{\odot}$ of amorphous carbon from clumped models. Both results are lower than our estimate. The discrepancy may be attributed to the value of $K_{\text{ext},V}$ which is affected by the species and size distribution of dust grains. Nozawa & Fukugita (2013) construct a graphite-silicate model with a power law size distribution, which is similar to the mixed models of Owen & Barlow (2015), and obtain $K_{\text{ext},V} = (3.7 \pm 0.5) \times 10^4 \text{ mag cm}^2 \text{ g}^{-1}$, which would make our estimation of dust mass being $0.498 M_{\odot}$ and effectively reduce the discrepancy.

According to the distribution of the nebular tracers, a similar clumped-shell geometry as described by Owen & Barlow (2015) can be applied to Monoceros SNR. The SN explosion cleared an inner region around the central point so it is free of dust now, whilst the ISD has been swept-up into the

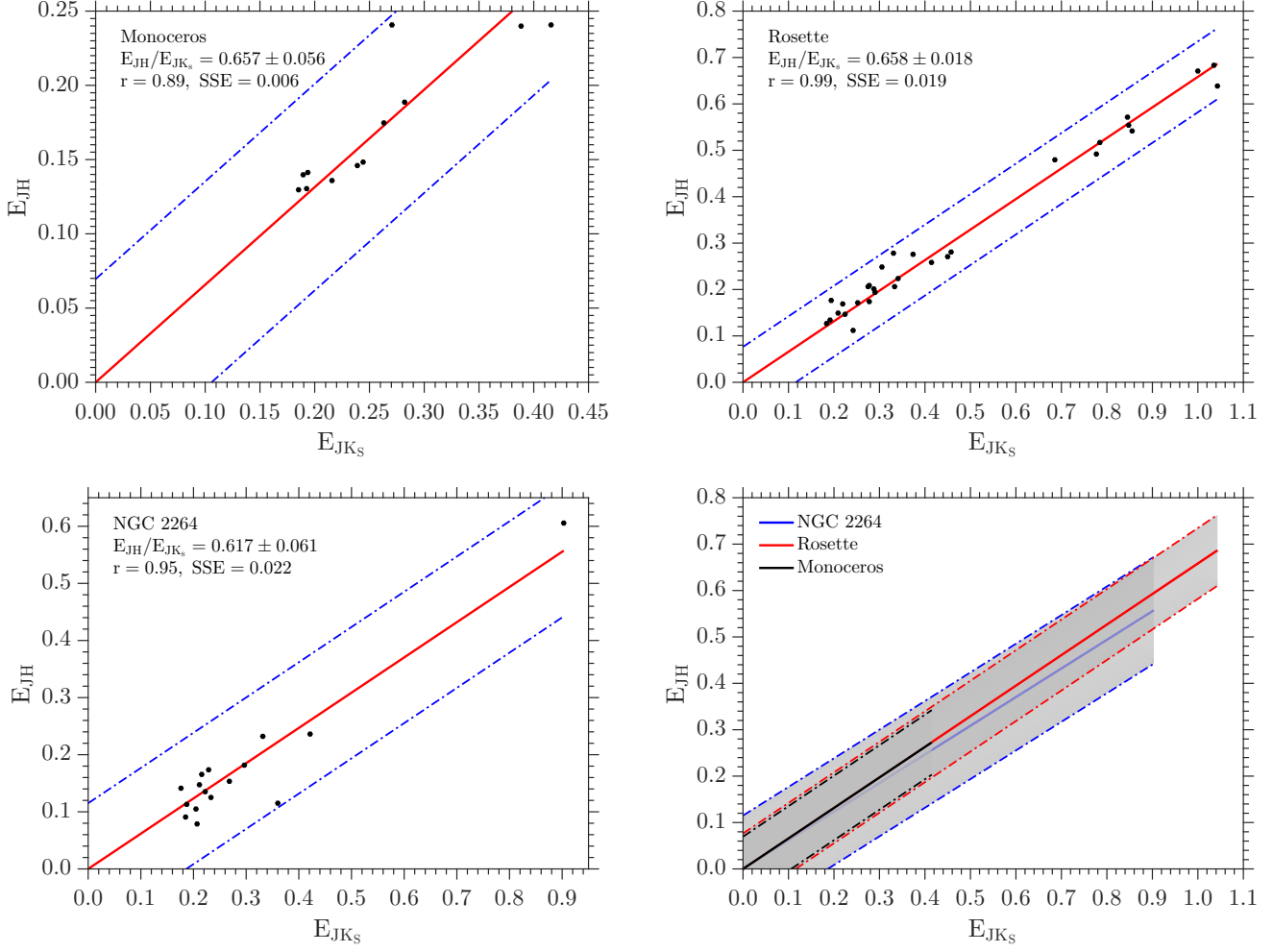


Figure 15. Color excess ratio, E_{JH}/E_{JKs} , for the three target nebulae and their comparison. The red solid line is the linear fitting result, and the blue dash lines bound the 3σ uncertainty region.

outer dense shell, i.e. the clumped shell. Figure 13(a) shows the lack of significant extinction in the central part of the SNR, consistent with the presumed scenario. The Monoceros SNR has an angular diameter of $220'$, corresponding to a radius of 63.36 pc at the derived distance of 1.98 kpc. We assume a circular shell for simplicity. The dust clumps start at inner radius, R_{in} . From Figure 10, it can be seen that the nebular extinction varies from about 0.01 to 0.15 in A_{Ks} . For a rudimentary estimation, an average extinction of 0.05 in the Ks -band is adopted that corresponds to 0.5 mag in A_V . Then the mass of the dust (M_{dust}) clumped in the shell is

$$\begin{aligned}
 M_{dust} &= \frac{0.5 \times \pi \times (R_{out}^2 - R_{in}^2) \times F_{fil}}{K_{ext,V}} \\
 &= \left(1073.595 - 0.26743 \left(\frac{R_{in}}{\text{pc}} \right)^2 \right) F_{fil} \text{ M}_{\odot}.
 \end{aligned} \tag{13}$$

Because our extinction map is incomplete for the SNR due to the lack of data, it is hard to determine the boundary of the inner ring. If the filling factor F_{fil} equals to 0.1 as Barlow et al. (2010), the dust

mass is from $38.65 M_{\odot}$ to $80.52 M_{\odot}$ if R_{in} is 50% to 80% of R_{out} estimated from Figure 13 (a). Since the supernova dust is usually on the order of a few percent to at most a couple of tenths solar mass, the dust mass is mostly contributed by normal ISD. This fact can be understood by the old age of the Monoceros supernova remnant able to sweep a large region of ISM. This result is also consistent with the fact that the near-infrared extinction law agrees with the mean law as discussed in previous section. In this case, the characteristics inhibited in the SN explosion is obliterated when the ISD dominates absolutely during the long evolution after explosion. This method can be improved by an extinction law covering a complete wavelength range instead of only the V -band. We will modify the method in further work.

7. SUMMARY

The goal of this work is to investigate the dust property of the SNRs from the nebular extinction and its law. The present work determines the distance and near-infrared extinction law of the Monoceros SNR and its nearby two nebulae – the Rosette Nebula and NGC 2264. By taking the stars in the corresponding sightlines as the extinction tracers, the distance of a nebula is found at the position of sharp increase of stellar extinction with distance. The stellar extinction is calculated by its color excess with the intrinsic color index derived from its stellar parameters (mainly T_{eff}) based on spectroscopic surveys. Its distance is calculated from the absolute magnitude fitted by the PARSEC model from $[\text{Fe}/\text{H}]$, T_{eff} and $\log g$ after subtracting interstellar extinction. The distance of Monoceros SNR is 1.98 kpc, larger than previous results. The distance of Rosette Nebula, 1.55 kpc, agrees with some of previous values. The large difference between these two nebulae, 0.4 kpc, implies little possibility that they are interacting with each other. For NGC 2264, the distance, 1.2 kpc, is slightly larger than previous results. The relative position of the three nebulae coincides with the Davies et al. (1978) result, i.e. the Monoceros SNR being the furthest and NGC 2264 the closest. The nebular extinction is derived by subtracting the foreground extinction which is calculated from a reference diffuse field with comparable Galactic latitude. The near-infrared extinction law of the Monoceros SNR as well as the two nearby nebulae shows no apparent difference with the mean near-infrared extinction law. This fact may be a piece of evidence for the universality of the near-infrared extinction law. On the other hand, the old age ($\sim 10^5$ yr) and the large mass ($\sim 50 M_{\odot}$ on average) of Monoceros SNR signify that the material of this SNR is absolutely dominated by the ISD other than the SN ejecta. The work needs to be extended to the UV/visual extinction law and a more accurate estimation of the property of the SNRs.

We thank Profs. Bruce Draine, Jian Gao, Aigen Li, Yong Zhang, and the anonymous referee for very helpful suggestions and stimulating comments. We thank Mengfei Zhang for technological help. This work is supported by NSFC through Projects 11373015, 11533002, and 973 Program 2014CB845702. This work makes use of the data from the surveys by LAMOST, SDSS/APOGEE, and 2MASS.

Software: PARSEC, CMD (v3.0; <http://stev.oapd.inaf.it/cmd>)

REFERENCES

- | | |
|--|--|
| <p>Alam, S., Albareti, F. D., Allende Prieto, C.,
et al. 2015, ApJS, 219, 12</p> | <p>Arendt, R. G., Dwek, E., Kober, G., Rho, J., &
Hwang, U. 2014, ApJ, 786, 55</p> |
|--|--|

- Barlow, M. J., Krause, O., Swinyard, B. M., et al. 2010, *A&A*, 518, L138
- Becker, W., & Fenkart, R. 1963, *ZA*, 56, 257
- Bevan, A., & Barlow, M. J. 2016, *MNRAS*, 456, 1269
- Bevan, A., Barlow, M. J., & Milisavljevic, D. 2017, *MNRAS*, 465, 4044
- Biscaro, C., & Cherchneff, I. 2016, *A&A*, 589, A132
- Bocchio, M., Marassi, S., Schneider, R., et al. 2016, *A&A*, 587, A157
- Bressan, A., Marigo, P., Girardi, L., et al. 2012, *MNRAS*, 427, 127
- Cohen, M., Wheaton, W. A., & Megeath, S. T. 2003, *AJ*, 126, 1090
- Cutri, R. M., Skrutskie, M. F., van Dyk, S., et al. 2003, *2MASS All Sky Catalog of point sources*.
- Davies, G. R., Lund, M. N., Miglio, A., et al. 2017, *A&A*, 598, L4
- Davies, R. D. 1963, *The Observatory*, 83, 172
- Davies, R. D., Elliott, K. H., Goudis, C., Meaburn, J., & Tebbutt, N. J. 1978, *A&AS*, 31, 271
- De Looze, I., Barlow, M. J., Swinyard, B. M., et al. 2017, *MNRAS*, 465, 3309
- Deng, L. 2014, in *IAU Symposium*, Vol. 298, *Setting the scene for Gaia and LAMOST*, ed. S. Feltzing, G. Zhao, N. A. Walton, & P. Whitelock, 269–280
- Deng, L.-C., Newberg, H. J., Liu, C., et al. 2012, *Research in Astronomy and Astrophysics*, 12, 735
- Draine, B. T. 2011, *Physics of the Interstellar and Intergalactic Medium*
- Ducati, J. R., Bevilacqua, C. M., Rembold, S. B., & Ribeiro, D. 2001, *ApJ*, 558, 309
- Dunne, L., Gomez, H. L., da Cunha, E., et al. 2011, *MNRAS*, 417, 1510
- Eisenstein, D. J., Weinberg, D. H., Agol, E., et al. 2011, *AJ*, 142, 72
- Gaia Collaboration, Prusti, T., de Bruijne, J. H. J., et al. 2016a, *A&A*, 595, A1
- Gaia Collaboration, Brown, A. G. A., Vallenari, A., et al. 2016b, *A&A*, 595, A2
- Girardi, L., Bertelli, G., Bressan, A., et al. 2002, *A&A*, 391, 195
- Girardi, L., Grebel, E. K., Odenkirchen, M., & Chiosi, C. 2004, *A&A*, 422, 205
- Gomez, H. L., Krause, O., Barlow, M. J., et al. 2012, *ApJ*, 760, 96
- Gottlieb, D. M., & Upson, II, W. L. 1969, *ApJ*, 157, 611
- Graham, D. A., Haslam, C. G. T., Salter, C. J., & Wilson, W. E. 1982, *A&A*, 109, 145
- Green, D. A. 2014, *Bulletin of the Astronomical Society of India*, 42, 47
- Griffin, M. J., Abergel, A., Abreu, A., et al. 2010, *A&A*, 518, L3
- Hester, J. J. 2008, *ARA&A*, 46, 127
- Hines, D. C., Rieke, G. H., Gordon, K. D., et al. 2004, *ApJS*, 154, 290
- Indebetouw, R., Matsuura, M., Dwek, E., et al. 2014, *ApJL*, 782, L2
- Jian, M., Gao, S., Zhao, H., & Jiang, B. 2017, *AJ*, 153, 5
- Johnson, H. L. 1962, *ApJ*, 136, 1135
- Katagiri, H., Sugiyama, S., Ackermann, M., et al. 2016, *ApJ*, 831, 106
- Leahy, D. A., Naranan, S., & Singh, K. P. 1986, *MNRAS*, 220, 501
- Lejeune, T., Cuisinier, F., & Buser, R. 1997, *A&AS*, 125, astro-ph/9701019
- Maiolino, R., Schneider, R., Oliva, E., et al. 2004, *Nature*, 431, 533
- Matsuura, M., Barlow, M. J., Zijlstra, A. A., et al. 2009, *MNRAS*, 396, 918
- Matsuura, M., Dwek, E., Meixner, M., et al. 2011, *Science*, 333, 1258
- Mészáros, S., Holtzman, J., García Pérez, A. E., et al. 2013, *AJ*, 146, 133
- Michalik, D., Lindegren, L., & Hobbs, D. 2015, *A&A*, 574, A115
- Miller, J. S. 1973, *ApJL*, 180, L83
- Mills, B. Y. 1974, in *IAU Symposium*, Vol. 60, *Galactic Radio Astronomy*, ed. F. J. Kerr & S. C. Simonson, 311
- Milne, D. K., & Aller, L. H. 1980, *AJ*, 85, 17
- Morgan, W. W., Hiltner, W. A., Neff, J. S., Garrison, R., & Osterbrock, D. E. 1965, *ApJ*, 142, 974
- Neugebauer, G., Habing, H. J., van Duinen, R., et al. 1984, *ApJL*, 278, L1
- Nozawa, T., & Fukugita, M. 2013, *ApJ*, 770, 27
- Nozawa, T., Kozasa, T., Habe, A., et al. 2007, *ApJ*, 666, 955
- Ott, S. 2010, in *Astronomical Society of the Pacific Conference Series*, Vol. 434, *Astronomical Data Analysis Software and Systems XIX*, ed. Y. Mizumoto, K.-I. Morita, & M. Ohishi, 139

- Owen, P. J., & Barlow, M. J. 2015, *ApJ*, 801, 141
- Pilbratt, G. L., Riedinger, J. R., Passvogel, T., et al. 2010, *A&A*, 518, L1
- Schultheis, M., Zasowski, G., Allende Prieto, C., et al. 2014, *AJ*, 148, 24
- Stassun, K. G., & Torres, G. 2016, *ApJL*, 831, L6
- Temim, T., Dwek, E., Arendt, R. G., et al. 2017, *ApJ*, 836, 129
- Walker, M. F. 1956, *ApJS*, 2, 365
- Wang, S., & Jiang, B. W. 2014, *ApJL*, 788, L12
- Watson, D., Christensen, L., Knudsen, K. K., et al. 2015, *Nature*, 519, 327
- Weingartner, J. C., & Draine, B. T. 2001, *ApJ*, 548, 296
- Wesson, R., Barlow, M. J., Matsuura, M., & Ercolano, B. 2015, *MNRAS*, 446, 2089
- Wheelock, S. L., Gautier, T. N., Chillemi, J., et al. 1994, NASA STI/Recon Technical Report N, 95
- Worley, C. C., de Laverny, P., Recio-Blanco, A., Hill, V., & Bijaoui, A. 2016, *A&A*, 591, A81
- Xiao, L., & Zhu, M. 2012, *A&A*, 545, A86
- Xue, M., Jiang, B. W., Gao, J., et al. 2016, *ApJS*, 224, 23
- Zhao, G., Zhao, Y.-H., Chu, Y.-Q., Jing, Y.-P., & Deng, L.-C. 2012, *Research in Astronomy and Astrophysics*, 12, 723